

Earth Surface Processes and Landforms



The impact of storm-triggered landslides on sediment dynamics and catchment-wide denudation rates in the southern Central Range of Taiwan following the extreme rainfall event of Typhoon Morakot

Journal:	<i>Earth Surface Processes and Landforms</i>
Manuscript ID	ESP-18-0338.R3
Wiley - Manuscript type:	Research Article
Date Submitted by the Author:	n/a
Complete List of Authors:	Chen, Chia-Yu; ETH Zurich, Department of Earth Sciences; National Taiwan University, Department of Geosciences; National Taiwan University, Department of Geography Willetts, Sean; ETH Zurich, Department of Earth Sciences Joshua West, A.; University of Southern California, Department of Earth Sciences Dadson, Simon; University of Oxford, School of Geography and the Environment Hovius, Niels; GFZ German Research Center for Geosciences, Geoarchives; Universitat Potsdam, Institute of Earth and Environmental Sciences Christl, Marcus; ETH Zurich, Department of Physics Shyu, J. Bruce H. ; National Taiwan University, Department of Geosciences
Keywords:	erosion, denudation, cosmogenic nuclides, landslides, Taiwan

SCHOLARONE™
Manuscripts

1
2
3
4
5
6
7
8
9
10
11
12
13
14
15
16
17
18
19
20
21
22
23
24
25
26
27
28
29
30
31
32
33
34
35
36
37
38
39
40
41
42
43
44
45
46
47
48
49
50
51
52
53
54
55
56
57
58
59
60

1 **The impact of storm-triggered landslides on sediment**
2 **dynamics and catchment-wide denudation rates in the**
3 **southern Central Range of Taiwan following the extreme**
4 **rainfall event of Typhoon Morakot**

6 Chia-Yu Chen^{a, b, c*}, Sean D. Willett^a, A. Joshua West^d, Simon Dadson^e, Niels
7 Hovius^{f, g}, Marcus Christl^h, J. Bruce H. Shyu^b

9 ^a Department of Earth Sciences, ETH Zurich, Sonnegstrass 5, 8092 Zurich,
10 Switzerland

11 ^b Department of Geosciences, National Taiwan University, No. 1, Sec. 4,
12 Roosevelt Rd., Taipei 106, Taiwan

13 ^c Department of Geography, National Taiwan University, No. 1, Sec. 4,
14 Roosevelt Rd., Taipei 106, Taiwan

15 ^d Department of Earth Sciences, University of Southern California, 3651
16 Trousdale Pkwy - Zumberge Hall 117, Los Angeles, CA 90089, USA

17 ^e School of Geography and the Environment, University of Oxford, South Parks
18 Road, Oxford, OX1 3QY, UK

19 ^f GFZ German Research Center for Geosciences, Telegrafenberg Potsdam
20 14473, Germany

21 ^g Institute of Earth and Environmental Sciences, University of Potsdam,
22 Karl-Liebkecht-Str. 24-25, 14476 Potsdam-Golm, Germany

23 ^h Department of Physics, Laboratory of Ion Beam Physics, ETH Zurich,
24 Otto-Stern-Weg 5, 8093 Zurich, Switzerland

25 *Corresponding to: chiayuchen@ntu.edu.tw

26

Abstract: Extreme erosion events can produce large short-term sediment fluxes. Such events complicate erosion rates estimated from cosmogenic nuclide concentrations in river sediment by providing sediment with a concentration different from the long-term basin average. We present a detrital ^{10}Be study in southern Taiwan, with multiple samples obtained in a time sequence bracketing the 2009 Typhoon Morakot, to assess the impact of landslide sediment on ^{10}Be concentrations ($N^{10}\text{Be}$) in river sediment. Sediment samples were collected from 13 major basins, 2 or 3 times over the last decade, to observe the temporal variation of $N^{10}\text{Be}$. Landslide inventories with time intervals of 5 to 6 years were used to quantify sediment flux changes.

A negative correlation between $N^{10}\text{Be}$ and landslide areal density indicates dilution of $N^{10}\text{Be}$ by landslide sediment. Denudation rates estimated from the diluted $N^{10}\text{Be}$ can be up to three times higher than the lowest rate derived from the same basins. Observed increases imply that 3 years after the passage of typhoon Morakot, fluvial channels still contain a considerable amount of sediment provided by hillslope landslides during the event. However, higher $N^{10}\text{Be}$ in 2016 samples indicate that the contribution from landslide sediment at the sampled grain size has decreased with time. The correlation between changes in $N^{10}\text{Be}$ and landslide area and volume is not strong, likely resulting from stochastic and complex nature of sediment transport. To simultaneously evaluate the volume of landslide-derived sediment and estimate the background denudation rate, associated with less impulsive sediment supply, we constructed a sediment-mixing model with the time series of $N^{10}\text{Be}$ and landslide inventories. The spatial pattern of

1
2
3
4
5
6
7
8
9
10
11
12
13
14
15
16
17
18
19
20
21
22
23
24
25
26
27
28
29
30
31
32
33
34
35
36
37
38
39
40
41
42
43
44
45
46
47
48
49
50
51
52
53
54
55
56
57
58
59
60

51 background erosion rate in southern Taiwan is consistent with the regional
52 tectonic framework, indicating that the landscape is evolving mainly in
53 response to the tectonic forcing, and this signal is modified, but not obscured
54 by impulsive sediment supply.

55

56 **Keywords**

57 erosion; denudation; cosmogenic nuclides; landslides; Taiwan

58

59 **Introduction**

60 Characterizing spatial patterns of denudation rates at multiple timescales
61 is essential for studying how landscapes evolve over time and space and can
62 help illuminate spatial and temporal variability in controlling factors, such as
63 tectonic and climate forcings and substrate properties. Many well-established
64 tools have provided ways to estimate denudation rates at different timescales,
65 such as erosion or cooling rates derived from thermochronometry averaging
66 over a timescale of millions of years (Reiners and Brandon, 2006), river loads
67 sampling sediment supply rates over tens of years (Syvitski and Milliman,
68 2007), and concentrations of cosmogenic radionuclides (CRNs) in detrital
69 sediment providing catchment-averaged denudation rates over hundreds to
70 tens of thousands of years (Granger et al., 2013; Portenga and Bierman,
71 2011). Over the past two decades, the latter, in particular the use of in-situ
72 ¹⁰Be CRN in quartz grains of river sediments, has emerged as one of the most
73 extensively applied of these tools (Granger et al., 2013). It has been used
74 globally to determine basin-wide denudation rates as samples are easy to
75 collect and the timescale is comparable with the timescale of a landscape

76 responding to a change in forcings (Kirby and Whipple, 2012).

77 The production rate of in-situ ^{10}Be CRN decays exponentially with depth
78 below the Earth's surface, and thus CRNs accumulate only when rocks or
79 sediments are brought into a near-surface production zone (a few meters
80 below the surface) by removal of overburden (Brown et al., 1995; Dunai,
81 2010). If the denudation rate is at steady state in a basin and sediments are
82 well mixed, so that all parts of a catchment's upstream area contribute
83 sediments proportional to their local denudation rate, then the bulk ^{10}Be
84 concentration ($N^{10}\text{Be}$) in quartz grains collected from river sediments
85 represents the spatially averaged $N^{10}\text{Be}$ of material harvested from the near
86 surface of the upstream catchment, and thus can be used to estimate the
87 basin-averaged denudation rate (Bierman and Steig, 1996; Granger et al.,
88 1996). However, in basins prone to landslides, the average $N^{10}\text{Be}$ may not be
89 representative of the long-term catchment-wide denudation rate (Niemi et al.,
90 2005; Sosa Gonzalez et al., 2017; Yanites et al., 2009) as a landslide can
91 easily excavate to a depth exceeding the ^{10}Be production zone providing
92 sediments with low or no $N^{10}\text{Be}$. When these sediments are delivered to the
93 river system, dilution of the $N^{10}\text{Be}$ can be detected in samples collected from
94 river sediments (Kober et al., 2012; West et al., 2014). Therefore, it is
95 important to assess possible recent dilution by landslide input when applying
96 the ^{10}Be approach to derive basin-wide denudation rates in
97 landslide-dominated basins. Although these recent dilutions perturb long-term
98 denudation signals (those associated with less punctuated hillslope sediment
99 supply), they also provide a way to track the export of event-associated
100 landslide sediment, provided that multiple samples are analyzed over time

101 following an event (West et al., 2014).

102 Here, we investigate a natural experiment provided by the impact of the
103 super-typhoon Morakot, in 2009 on southern Taiwan. The event brought
104 exceptional rainfall and triggered several thousand landslides in the southern
105 Central Range (Fig. 1A) (Lin et al., 2011), yielding an unusual pulse of
106 sediment to the fluvial system and altering the sediment transport regime
107 (Huang and Montgomery, 2013). Studies of suspended sediment records from
108 river gauging stations have provided quantitative examples showing that fluvial
109 system is impacted for years to decades by the input of sediments supplied
110 from landslides triggered by earthquakes or intensive rainfall events (Dadson
111 et al., 2004; Hovius et al., 2011; Howarth et al., 2012; Huang and Montgomery,
112 2013; Marc et al., 2015; Wang et al., 2015). For example, the 1999 M_w 7.6
113 Chi-Chi earthquake in central Taiwan and the 2008 M_w 7.9 Wenchuan
114 earthquake in China both triggered tens of thousands of landslides that
115 enhanced sediment supply to fluvial systems substantially, resulting in
116 increases in suspended sediment flux for 6 years or longer (Hovius et al., 2011;
117 Wang et al., 2015). As a measure of landscape response, variability in $N^{10}Be$
118 in sediment is expected to behave similarly, although the timescale of
119 restoration to background values will depend on the delivery of landslide
120 sediment and thus may differ from the timescale of suspended sediment
121 records. Numerical modeling provides a theoretical basis for treating this
122 problem (Niemi et al., 2005; Yanites et al., 2009), but there have been few
123 observational tests, in part because proper tests require a time series of
124 measurements across an unpredictable event.

125 This study is based on systematic sediment sampling at various times,

126 incidentally bracketing the Morakot typhoon, providing a valuable opportunity
127 to detect its impact on $N^{10}Be$ in river sediments of the landslide-affected region
128 in southern Taiwan. To supplement these data, we obtained landslide
129 inventories for different time periods over the same time interval as the $N^{10}Be$
130 time series. To relate these data and aid interpretation, we constructed a
131 sediment-mixing model based on landslide mapping to constrain the
132 background erosion rate and variation in the fraction of landslide debris in river
133 sediments.

135 **Setting: the southern Central Range and Typhoon Morakot**

136 The island of Taiwan has been built on a complex arc-continent collision
137 boundary, where the Luzon arc of the Philippine Sea Plate moves
138 northwestward at the current rate of 82 mm/yr colliding with the continental
139 margin of the Eurasia Plate (Chai, 1972; Ho, 1986; Yu et al., 1997)(Inset in Fig.
140 1A). As a transition zone between oceanic subduction and the arc-continent
141 collision that forms the Taiwan orogen, the southern Central Range represents
142 the initial collision stage of the orogen and is characterized by transient
143 landscapes and a complex uplift pattern (Chang et al., 2009; Chen and Willett,
144 2016; Giletycz et al., 2015). Thermochronometry and $N^{10}Be$ in river sediments
145 show a northward increasing erosion rate from <1 to 3 mm/yr over million-year
146 and millennial timescales along the eastern flank of the range (Fellin et al.,
147 2017).

148 The 2009 typhoon Morakot was the most destructive typhoon in the
149 recorded history of Taiwan (1897 - recent). It produced extensive rainfall
150 concentrated in southern Taiwan with a record of 2146.5 mm rainfall in 48 hrs,

1
2
3
4
5
6
7
8
9
10
11
12
13
14
15
16
17
18
19
20
21
22
23
24
25
26
27
28
29
30
31
32
33
34
35
36
37
38
39
40
41
42
43
44
45
46
47
48
49
50
51
52
53
54
55
56
57
58
59
60

151 triggering several thousand landslides that strongly impacted several basins in
152 the southern Central Range (Fig. 1A) (Lin et al., 2011). Many of these
153 landslides connected directly with the river channel network (West et al.,
154 2011), supplying abundant sediment to the fluvial system, and giving rise to an
155 increase in sediment flux even at low-flow conditions in subsequent years
156 (Huang and Montgomery, 2013).

157
158 **Cosmogenic nuclides for erosion rate**

159 To estimate the pattern of background long-term denudation rates in the
160 southern Central Range and to assess the impact of mass wasting due to
161 typhoon Morakot, we collected samples from 13 major basins draining the
162 southern Central Range over a time interval bracketing the typhoon. Most
163 basins were sampled three times. The first suite of samples was collected with
164 no anticipation of the Morakot event, in the spring of 2006, and is composed of
165 12 samples with sample numbers initialed ST (Fig. 1B and Table 1 and 2). The
166 post-Morakot samples were collected in late 2012, and again in early
167 2015/2016 for a total of 26 samples numbered with initials TW or using
168 abbreviations of basins (Fig. 1B and Table 1 and 2). The basins were
169 numbered with initials W and E for western and eastern basins, respectively,
170 and numbers increasing from south to north reflecting relative distances
171 between the outlets and the southern tip of the island (Table 2).

172 Samples were sieved into different grain-size fractions, and only the
173 fraction of 250-710 μm was analyzed in this study. Clean quartz grains were
174 obtained following the protocol described in Fellin et al. (2017). The purification
175 of ^{10}Be was achieved by first dissolving 50-100 g of quartz grains after adding

~0.2 mg of a commercial carrier solution (Scharlau) and then using both cation and anion chromatography to remove other elements (Ivy-Ochs, 1996). The Be was precipitated as $\text{Be}(\text{OH})_2$ and transferred to BeO at 1000 °C. Targets for accelerator mass spectrometry (AMS) measurements were prepared with an addition of ~3 mg Nb powder and measured mostly at ETH Zurich Tandy facility (Christl et al., 2013; Müller et al., 2010), while 4 sediment samples (ST02, ST09, ST12, and ST15) were processed and measured at SUERC NERC Cosmogenic Isotope Analysis Facility. Measurements carried out at ETH were normalized to an in-house secondary ^{10}Be standard S2007N with a nominal $^{10}\text{Be}/^9\text{Be}$ ratio of 28.1×10^{-12} (Kubik and Christl, 2010) calibrated with a primary standard ICN 01-5-1 with the $^{10}\text{Be}/^9\text{Be}$ ratio of 2.709×10^{-11} (Nishiizumi et al., 2007) and a ^{10}Be half-life of 1.387 ± 0.012 Ma (Chmeleff et al., 2010; Korschinek et al., 2010), whereas at SUERC, measurements were normalized to the NIST SRM-4325 ^{10}Be standard with a revised nominal $^{10}\text{Be}/^9\text{Be}$ ratio of 2.79×10^{-11} (Nishiizumi et al., 2007).

Normalized ratios were then corrected with corresponding blanks. As several blanks were processed with some batches, we used error-weighted mean blanks for blank corrections (Table 1). A χ^2 test was used to verify the reliability of each measurement (Ward and Wilson, 1978) as the $N^{10}\text{Be}$ is relatively low in many surface materials from Taiwan owing to the high denudation rate and frequent landslides. One degree of freedom at 95% confidence level gives a critical χ^2 value of 3.84, which means if the sample has a χ^2 value greater than 3.84, it is significantly different from the blank and can be used to derive a basin-wide erosion rate (ϵ) with the following equation (Brown et al., 1995):

$$N = \frac{1}{\varepsilon} \left(\frac{P_n}{\rho / \Lambda_n} + \frac{P_{ms}}{\rho / \Lambda_{ms}} + \frac{P_{mf}}{\rho / \Lambda_{mf}} \right) \quad (1)$$

where N is the nuclide concentration, P is the mean basin ^{10}Be production rate, ρ is the rock density (set at 2.7 g/cm^3) and Λ is the attenuation length ($\Lambda_n = 160$, $\Lambda_{ms} = 1500$, $\Lambda_{mf} = 4320 \text{ g/cm}^2$ (Braucher et al., 2011)). Subscripts n , ms , and mf denote production pathways associated with neutrons, and slow and fast muons, respectively. Production rates at each pixel were calculated from a 40 m digital elevation model (DEM) of Taiwan according to the altitude, latitude and local topographic shielding, and the mean basin production rate is the average of production rates of all pixels in a basin. Topographic shielding was calculated with a MATLAB script in TopoToolbox (Schwanghart and Scherler, 2014) following the method introduced by Dunne et al. (1999). The neutron production rate was scaled for latitudinal and altitudinal variations following Stone (2000) to a reference production rate of 4.01 at/g measured at sea level and high latitude (Borchers et al., 2015), whereas muon production rates were scaled to altitudinal variation only following Braucher et al. (2011). The bedrock in the study area is relatively homogeneous and mostly composed of Miocene slate and metasandstone with some exposures of slightly higher-grade metamorphic schist of Eocene to Miocene age in basins towards the north. All formations are assumed to supply sufficient and similar quantities of quartz to river sediment. Therefore, we only applied a minor correction for rock type by removing the sediment contribution of quartz-free marbles. We used a Monte Carlo approach to estimate the total uncertainty of the denudation rate, including the analytical uncertainty of the AMS measurement, 2.5% in P_n , 50% in P_{ms} and P_{mf} , and 9% in scaling scheme. For a sample measured more than

once, we calculated the error-weighted mean denudation rate using measurements passing the χ^2 test.

Landslide mapping and analysis

To assess the impact of landslide sediment on $N^{10}Be$, we quantified landslide distribution and areal density. We mapped landslides using Landsat imagery captured in 2001, 2007, 2013 and 2015 before the typhoon season, and 2009 after the typhoon season, such that we compiled three landslide inventories for periods of pre-2001, 2001-2006, 2007-2012 and 2010-2014 to have similar interval lengths with timing comparable to our ^{10}Be measurements (Fig. 1A). Based on the spectral reflectance of the earth's surface features, landslides were identified by the surface changes from vegetation cover to reflective bare bedrock or sediment in the imagery. For landslides expanding in area over time through reactivation, only new parts were mapped during each mapping interval. The resolution of Landsat imagery is 30 meters, which prohibits accurate distinction between landslide scars and deposits, and thus the mapped landslides include both components. To estimate the scar area of each landslide, we used the size ratio between scar and deposit areas proposed by previous studies, i.e. 1.1 for small, shallow soil and bedrock mixed landslides with landslide area less than $10^5 m^2$, and 1.9 for larger bedrock-involving landslides (Larsen et al., 2010). The landslide areal density (LAD) of each basin is defined as the total scar area of newly detected landslides divided by basin area over each time period. We assumed that this represents a quantitative estimate of the maximum amount of newly available sediment with low $N^{10}Be$ that will perturb the long-term mean basin $N^{10}Be$.

Landslide depths were estimated to calculate the mean $N^{10}Be$ of landslide sediment over each time period. The mean depth of a landslide (d_{ls}) was calculated by dividing the scar area by the volume, as:

$$d_{ls} = \frac{\alpha A^\gamma}{A} \quad (2)$$

where A is the scar area of a mapped landslide, and α and γ are the intercept and scaling exponent of the area-volume scaling relationship ($V = \alpha A^\gamma$) with global values as $\alpha = 0.146$ and $\gamma = 1.33$ for mixed landslides, and $\alpha = 0.234$ and $\gamma = 1.41$ for bedrock landslides (Larsen et al., 2010; Marc and Hovius, 2015). The uncertainty of each d_{ls} (σ_d) was estimated with a Monte Carlo simulation considering uncertainties of 20 % in mapping error, 0.005 and 0.02 in α , and 0.005 and 0.03 in γ for mixed and bedrock landslide scars, respectively (Larsen et al., 2010; Marc et al., 2015). This estimation yields an uncertainty of mean landslide depth of about 30 % on average.

Results

Time series of ^{10}Be concentrations and derived denudation rates

The measured $N^{10}Be$ ranged from $0.87 \pm 0.47 \times 10^3$ to $56.19 \pm 2.71 \times 10^3$ at/g (Table 1 and 2) and revealed both temporal and spatial variations. Concentrations for samples collected in 2006 and 2015/2016 were higher with a factor of 1.05-2.42 than those for samples collected in 2012 in all basins except basins LP (W5) and LiL (W4), where results showed a slight trend in the opposite direction. Spatially, $N^{10}Be$ increased from north to south and had higher values in western basins to the south of the LiL basin (W4) (Table 2). Although denudation rate is not a linear function of $N^{10}Be$ as the mean

production rate varies among basins, the basin-wide denudation rates mirror $N^{10}\text{Be}$ with rates ranging between 0.06 and 4.55 mm/yr (Table 2). To compare the degree of impact from landslide sediment among basins, in each basin, we calculated ratios of each ^{10}Be -derived denudation rate to the lowest rate for that basin, which we assumed to have the least impact of landslide dilution (Fig. 2).

In eastern basins (Fig. 2 and Table 2), samples collected in 2006 yielded the lowest rates for basins DN (E7), DW (E2) and AS (E1), whereas in basins CP (E6), TML (E5), CL (E4) and DC (E3), samples collected in 2016 yielded the lowest rates. Samples collected in 2012 yielded the highest rates in all basins. The rate increased by a factor of 3 from 2006 to 2012 in basins DN (E7) and DW (E2), with these showing the largest variations in all studied basins. The AS (E1) basin showed the smallest temporal variation in denudation rate. Basins CP (E6), TML (E5), CL (E4), and DC (E3) had moderate variations in denudation rate, but samples from these sites always yielded higher rates compared to other basins.

We obtained fewer data from western basins (Fig. 2 and Table 2). Unfortunately, we did not have a pre-Morakot sample for the AL basin (W6), which was the most strongly impacted by the 2009 typhoon. The sample collected in 2012 yielded a rate of $4.55^{+2.41}_{-1.29}$ mm/yr, which was the highest rate obtained in this study. Basins LP (W5) and LiL (W4) were the only two basins that show decreases in rate from 2006 to 2012. Further south, the variation in denudation rate was small over time in basins SM (W3), FS (W2), and FK (W1), but the rates were one order of magnitude lower than those of northern basins.

299

300 ***Changes of landslide areal density and mean landslide depth scale***

301 Prior to the Morakot event (2001-2006), landslide areal density (LAD)
 302 ranged from 0 to 1.2 % (Fig. 2 and Table 3). Most basins had pre-Morakot LAD
 303 less than 0.3 %, whereas basins TML (E5), CL (E4), and AL (W6) had higher
 304 values (0.67-1.2 %). During the period of 2007-2012, which includes the
 305 Morakot event, LAD increased substantially in all basins. The TML (E5) basin
 306 was the most strongly impacted basin where the LAD increased from 1.2 % to
 307 4.46 %. In the adjacent basins (AL (W6), LP (W5), LiL (W4), and CL (E4)), LAD
 308 also rose to greater than 2 %. The largest changes in LAD, however,
 309 happened in western basins LP (W5), LiL (W4), and SM (W3), where fewer
 310 landslides occurred in the time period prior to Morakot. The LAD increased by
 311 a factor of 15 to 32 in these basins, whereas the LAD increased by a factor of 2
 312 to 10 in other basins. Over the period of 2010 to 2014, the LAD dropped but
 313 still had a higher value than that over the first period in all basins except the
 314 DN basin (E7), where the LAD increased to its greatest value (0.54%).

315 If landslides are drawn from the same magnitude-frequency distribution,
 316 then the average and maximum landslide magnitudes likely increase as total
 317 landslide number increases (Malamud et al., 2004). In this case, we expect an
 318 increase in mean landslide depth (\bar{d}_{ls}) as it is calculated from the area-volume
 319 relationship of landslides (Fig. 2 and Table 3). Landslides occurring over the
 320 period of 2001-2006 had a \bar{d}_{ls} of less than 3 m, except in basin DW (E2),
 321 which had a \bar{d}_{ls} of around 3.7 m. As the Morakot event triggered many large
 322 landslides, the \bar{d}_{ls} increased over the period of 2007-2012 in all basins. Many
 323 basins had a \bar{d}_{ls} estimated to be greater than 5 m (basins AL (W6), LP (W5),

LiL (W4), TML (E5), DC (E3), and DW (E2)), and the largest average landslide depth was calculated to be about 12 m in the TML basin (E5). Over the period of 2010-2014, after Morakot, landslides were shallower with the mean depth inferred to be mostly under 2 m.

328

329 ***Correlation between changes in ^{10}Be concentration and landslide***

330 ***occurrence***

331 Overall, our results show that N^{10}Be and erosion rate vary with landslide
332 occurrence frequency metrics, including LAD. To explore the correspondence,
333 we plotted N^{10}Be against LAD (Fig. 3) for data of 2006, 2012 and 2015/2016.
334 The plots show a moderate negative correlation between N^{10}Be and LAD with
335 Pearson correlation coefficients (R) of about -0.5 (Table S1). If we drop the
336 data of basins SM (W3), FS (W2) and FK (W1) given that their N^{10}Be is one
337 order of magnitude higher than other basins, the strength of the correlation is
338 weaker for 2012 ($R=-0.27$). This weak correlation appears to be caused by the
339 increases of N^{10}Be in basins LP (W5) and LiL (W4) after the Morakot event. If
340 we drop the data of these two basins, the correlation is stronger ($R=-0.55$). In
341 addition, LAD was further classified as shallow or deep (LAD_s or LAD_d), where
342 we assume that larger landslides are deeper and divide landslides into two
343 groups with a boundary of 10^5 m^2 . The correlation between N^{10}Be and LADs is
344 similar to that between N^{10}Be and LAD, while there is almost no correlation
345 between N^{10}Be and LAD_d .

346 We also calculated the normalized changes in N^{10}Be ($\text{N}\Delta\text{C}$) over the
347 periods of 2006-2012 and 2006-2015/2016, and compared the changes to
348 other landslide factors, including normalized changes in total landslide scar

area ($N\Delta IsA$) and total landslide volume ($N\Delta IsV$). $N\Delta IsA$ and $N\Delta IsV$ were also classified as normalized changes in shallow or deep landslide scar area ($N\Delta IsA_s$ or $N\Delta IsA_d$) and volume ($N\Delta IsV_s$ or $N\Delta IsV_d$) (Fig. 4 and Table S2). The normalized changes were calculated by subtracting the 2006 values from the later values and normalized with the 2006 values. Over the period of 2006-2012, omitting basins LP and LiL which show $N^{10}Be$ changes in the opposite direction, $N\Delta C$ has a weak positive correlation with $N\Delta IsA$ and $N\Delta IsV$ except in the cases of $N\Delta IsA_d$ and $N\Delta IsV_d$, which have a strong positive and a weak negative correlation with $N\Delta C$, respectively. Over the period of 2006-2015/2016, $N\Delta C$ has a moderate negative correlation with $N\Delta IsA$ and $N\Delta IsV$, a strong negative correlation with $N\Delta IsA_s$ and $N\Delta IsV_s$, and no correlation with $N\Delta IsA_d$ and $N\Delta IsV_d$.

If $N^{10}Be$ in detrital sediments was diluted by sediment provided by landslides, we would expect that the larger increases in landslide activity would correspond to larger decreases in $N^{10}Be$. Surprisingly, we found the correlation between changes in $N^{10}Be$ ($N\Delta C$) and changes in scar area and volume of landslide ($N\Delta IsA$ and $N\Delta IsV$) over the period of 2006-2012 has a trend opposite to what we would expect (Fig. 4). The positive correlation over the period demonstrates that the relationship between the changes in $N^{10}Be$ and landslide activity is not simple or is not resolvable by current data. However, all basins still have negative $N\Delta C$ values when landslide activity increases, consistent with dilution of ^{10}Be by low concentration landslide sediments. The complication in the relationship could arise from many causes, such as landslide mapping errors, disequilibrium of ^{10}Be at the surface due to landslides occurred before the study period, and stochastic and complex

374 nature of sediment transport in different river systems. The last is likely as
375 extensive sediment aggradation was found in the river channels even several
376 years after the Morakot event. Estimating the degree of sediment dilution
377 would permit a better estimation of the long-term erosion rates and give insight
378 into the dynamics of sediment transport.

379

380 **Sediment-mixing model**

381 The samples we collected at the outlet of a basin were mixtures of
382 sediments from hillslope eroding at a long-term background erosion rate, and
383 sediments provided from recent landslides. $N^{10}Be$ in a sample thus can help to
384 quantify the mixing proportion of these two sources of sediments, if we can
385 reasonably estimate the mean $N^{10}Be$ in each component. With samples
386 collected repeatedly at the same place, we can obtain the mixing proportion at
387 different times. If the background erosion rate remains constant, we can
388 evaluate the differences in mass of landslide sediments in the channel system
389 and quantify the degree of ^{10}Be dilution by landslide sediment in each sample.
390 To achieve this, we constructed a simple sediment-mixing model with the
391 objective of constraining the range of the background erosion rate.

392 In the mixing model, we followed Yanites et al. (2009) in treating sediment
393 yield from a basin as a mixture of sediment from hillslopes eroding at some
394 mean, background rate (E_b) and sediment derived from recent event-triggered
395 landslides. We note that E_b describes the long-term average amount of
396 material being removed from the surface in each year, including erosion
397 associated with diffusive hillslope processes such as soil creep, as well as
398 erosion from background rates of landslide activity, provided that individual

landslides are small enough to be averaged by the sediment collection processes. In each model, we assumed an initial range of background erosion rate from 0.005 to 8 mm/yr. Sweeping through values of E_b from within this range, we calculated the expected $N^{10}\text{Be}$ as a mixture of sediment contributed from background erosion with mean concentrations corresponding to E_b (\bar{N}_b) and landslide sediment with a lower mean $N^{10}\text{Be}$ (\bar{N}_{ls}). These two endmembers are mixed to calculate the expected erosion rate (E_{mix}) that would be inferred from a catchment-wide average concentration measurement:

$$E_{mix} = \frac{1}{N_{mix}} \left(\frac{P_n}{\rho / \Lambda_n} + \frac{P_{ms}}{\rho / \Lambda_{ms}} + \frac{P_{mf}}{\rho / \Lambda_{mf}} \right) \quad (3)$$

with the mixed $N^{10}\text{Be}$ (N_{mix}) defined as:

$$N_{mix} = \bar{N}_{ls} \times F_{ls} + \bar{N}_b \times (1 - F_{ls}) \quad (4)$$

where F_{ls} is the fraction of landslide sediment, ranging from 0 to 1 with an increment of 0.001, such that we obtained 1000 mixing samples and E_{mix} values for each assumed E_b . In the case of no sediment supplied from landslides, $F_{ls} = 0$, E_{mix} will equal to E_b . Otherwise, E_{mix} increases as F_{ls} increases. When sediments all come from landslides, $F_{ls} = 1$, E_{mix} is determined by \bar{N}_{ls} . There is a trade-off between F_{ls} and E_b as this controls the $N^{10}\text{Be}$ of the mixed sample.

We applied this sediment-mixing model for the three time periods for which we have ^{10}Be data, i.e. pre-Morakot (2006), immediately post Morakot (2012), and 5-6 years after Morakot (2015/2016). \bar{N}_{ls} is almost impossible to measure directly given the large number of landslides in a basin. Instead, we estimated it by using size, depth, and location of all individual landslides over each period based on the landslide inventories. The model is initiated by

determining the initial $N^{10}\text{Be}$ at the surface (N_0) for each pixel in a basin. For a given E_b , we calculated the steady-state $N^{10}\text{Be}$ at the surface with equation (1). As $N^{10}\text{Be}$ is a depth function, to account for the effect of pre-existing landslides before 2006, where N_0 was unlikely to reach the secular equilibrium, we updated the $N^{10}\text{Be}$ at the surface after the landsliding according to the 2001 landslide inventory. The new $N^{10}\text{Be}$ at each landslide pixel was calculated based on N_0 and the depth of pre-2001 landslide (z):

$$N = N_0 e^{-z\rho/\Lambda} \quad (5)$$

Therefore, the model started from 2001 and with the time step of one year ($t=1$). In each time step, and at each pixel, we calculated the mean $N^{10}\text{Be}$ of eroded sediments (N_b) according to the background erosion by integrating the $N^{10}\text{Be}$ from the surface to the eroded depth ($d = E_b \times t$) and dividing by the depth:

$$N = \left(\int_0^d N_0 e^{-z\rho/\Lambda} dz \right) / d \quad (6)$$

\bar{N}_b , is the average $N^{10}\text{Be}$ of removed sediments. We then updated the surface $N^{10}\text{Be}$ to reflect the background erosion rate. If a landslide inventory was available in a time step, we calculated the mean $N^{10}\text{Be}$ at each pixel where a landslide had been mapped (N_{ls}) by replacing d with d_{ls} in equation (6). **Error! Reference source not found.**, and calculated the mean $N^{10}\text{Be}$ (\bar{N}_{ls}) of total landslide material in a basin. We kept the surface $N^{10}\text{Be}$ updated after removal of landslide material to avoid overestimation of $N^{10}\text{Be}$ in the following time steps. To account for the uncertainty in landslide depth, we repeated the procedure with values of $d_{ls} \pm \sigma_d$ (Fig. S1-S13).

447 ***Ranges of background denudation rates and contribution of landslide*** 448 ***sediment and their implications***

449 The range of background denudation rates (E_b) and the fraction of
 450 landslide debris in samples (F_{ls}) were constrained by combining our
 451 ^{10}Be -derived rates (E_m) with the sediment-mixing models. For each basin and
 452 sample collected in each time window (2001-2006, 2007-2012, and
 453 2010-2014), the model predicted a series of curves showing the erosion rate of
 454 the combined sediment, E_{mix} (black and grey curves in upper panels in Fig.
 455 S1-S13). Combining the ^{10}Be derived rate, E_m , with its model (red solid and
 456 dash lines in upper panels in Fig. S1-S13), we obtained a range of E_b as a
 457 function of F_{ls} between 0 and 1 (blue lines in lower panels in Fig. S1-S13) from
 458 intersections of E_m and E_{mix} (upper panels in Fig. S1-S13) as E_{mix} calculated
 459 based on different values of E_b should equal to E_m . Each model reveals a
 460 range of E_b , but only the overlap of ranges of all periods is permissible (orange
 461 shades in lower panels in Fig. S1-S13) as E_b represents a long-term
 462 background erosion rate and thus is not likely to change over this short period
 463 of time.

464 The model with multiple ^{10}Be measurements over time provides
 465 constraints on the background erosion rate, E_b and, simultaneously, gives an
 466 estimate of the fraction of landslide material, F_{ls} , of each sample. Overall, the
 467 results show that in a model with a higher E_m and a lower \bar{N}_{ls} tends to result in
 468 a larger range of E_b (e.g. the model of the DN basin over the 2001-2006
 469 period), whereas with a lower E_m and a higher \bar{N}_{ls} the inferred range of E_b is
 470 smaller (e.g. the model of the DN basin over 2001-2006 period) (Fig. S1). We
 471 summarized the permissible ranges of E_b and F_{ls} of each basin and plotted

472 them as a time series showing changes of landslide fraction in samples from
 473 basins over time (Fig. S14). Some basins have better constraints on E_b and F_{ls}
 474 resulting from high variability in E_m and \bar{N}_{ls} over time, such as basins DN (E7),
 475 CL (E4), and DW (E2). The southwestern basins (FK (W1), FS (W2), and SM
 476 (W3)) have lower E_b and similar ranges of F_{ls} over time. In the AS basin (E1),
 477 E_b was determined by E_m in 2006 as there were no or very few landslides,
 478 such that these were too small to be identified from Landsat imagery over the
 479 period of 2001-2006. Our ^{10}Be data do not provide good constraints on E_b and
 480 F_{ls} in basins CP (E6), TML (E5), and AL (W6) because E_m is always high, and
 481 \bar{N}_{ls} is always low.

482 Although models do not always result in confined ranges of E_b for given
 483 measurements, if F_{ls} can be reasonably estimated, we can further confine the
 484 range of permissible E_b . For example, in basins SM (W3), FS (W2), and FK
 485 (W1), where LAD is less than 0.1% over the period of 2001-2006, lower values
 486 of F_{ls} could be expected from our first sample suite, and thus E_b in these
 487 basins should be closer to the upper limit. Conversely, in basins TML (E5), CL
 488 (E4), and AL (W6), where the LAD is larger than 3.3 % during the period of
 489 2007-2012, the samples collected in 2012 have a higher chance of containing
 490 more landslide sediments, so we could expect the upper limits of E_b are lower.
 491 As can be seen from these examples, although the actual F_{ls} is hard to
 492 parameterize from LAD, the mapped landslide density still provides some
 493 insights into the most likely E_b , i.e. whether the true E_b is close to the upper or
 494 the lower limit of the estimated range. On the other hand, if E_b is well
 495 constrained by the model results, as in some basins in our study, the model
 496 can be used to directly measure the removal of landslide sediments in a basin

1
2
3
4
5
6
7
8
9
10
11
12
13
14
15
16
17
18
19
20
21
22
23
24
25
26
27
28
29
30
31
32
33
34
35
36
37
38
39
40
41
42
43
44
45
46
47
48
49
50
51
52
53
54
55
56
57
58
59
60

with future ^{10}Be measurements.

Discussion

Transport of landslide sediment and its impacts on ^{10}Be derived denudation rates

N^{10}Be and LAD have a negative correlation, indicating that the N^{10}Be was affected by the increase of landslide activity (Fig. 3). To explore the dynamics of mass transport following the Morakot event, we used the measured N^{10}Be as a metric to calculate the ratio of sediment mass at two different times based on an end-member mixing model (West et al., 2014). Our results show that in most of the basins, the ratios of sediment mass contributions in 2012 relative to the mass in 2006 and 2016 are larger than 1, indicating there was still a large amount of sediment accumulated in the river channel 3 years after the Morakot event (in 2012), but that the amount decreased significantly in 2016 (Fig. S15).

In the two exceptional basins, LP (W5) and LiL (W4), the LAD increases from less than 0.2 % over the period of 2001-2006 to greater than 2.4 % over the period of 2007-2012, indicating that significant dilution of N^{10}Be was present in the samples collected in 2012 (Table 3). However, instead of observing increases in the sediment mass ratios, we found increases in N^{10}Be , implying decreases in dilutional sediment mass (Figs. 2, S15 and Table 2). The drainage area of these two basins is relatively small, especially basin LP (W5) whose ^{10}Be derived rate in 2012 was obtained by area-weighting the rates derived from two samples (TW12-18 and TW12-19) collected from two upstream branches with drainage areas of 40 and 70 km^2 (Fig. 1B and Table

2). Therefore, we expect that the lower rates derived from these samples after Morakot may have been due to insufficient sediment mixing. These samples might sample shallow parts of local landslide sources where $N^{10}\text{Be}$ was high, which in turn implies that these basins were eroding unsteadily (Yanites et al., 2009). Alternatively, the $N^{10}\text{Be}$ might be perturbed by old landslide material accumulated on hillslopes (colluvium) that was flushed into the fluvial system during the Morakot event. In the field, we found extensive landslide deposits accumulated on hillslopes in the upstream area of the catchment captured by the sample TW12-18, indicating that the increase in $N^{10}\text{Be}$ after the Morakot event was most likely explained by the excavation of old landslide material.

Apart from basins LP (W5) and LiL (W4), other basins show decreases in $N^{10}\text{Be}$ and sediment mass from 2006 to 2012, which are likely related to Morakot and subsequent events as the LAD also increases noticeably over the period of 2007-2012 (Fig.2 and Tables 2 and 3). ^{10}Be derived rates in 2012 can be 2 to 3 times higher than the lowest rate calculated for each catchment, and the sediment mass can increase by more than 20 times in basins where landslides occurred extensively (Figs. 2 and S15). We also note that basins CP (E6), TML (E5), CL (E4), and DC (E3) have higher ^{10}Be derived rates compared to their adjacent basins prior to the period of 2007-2012 (Table 2). Given that the LAD for these basins is also higher than that of other adjacent basins, it seems that the majority of transported sediments were supplied from landslides over the decade prior to sampling in 2006 (Table 3). The high ^{10}Be derived rates in 2006 were most likely perturbed by landslides triggered by Typhoon Haitang that hit Taiwan in 2005. The contribution of landslide sediment seems to decrease as both the ^{10}Be derived rate and the LAD

decrease in 2016 (Fig. 2). This change implies that the landslide sediments generated during Morakot are depleting or have become disconnected from the fluvial system over time. We also note that there were many intense rainfall events in 2012, while it was relatively dry in 2014 and 2015 (Fig. 2), so that the different degrees of ^{10}Be dilution between the 2012 and 2016 sample suites may result from different frequencies of intense rainfall events, when more landslide sediments are flushed into the fluvial system. In this case, the less diluted N^{10}Be do not necessarily indicate that the influence of the Morakot event is almost terminated, but could signal instead that less of the Morakot-associated landslide material was delivered to the fluvial system in the years between 2012 and 2016. Another heavy rainfall event without newly occurred landslides could still result in significant dilution of N^{10}Be if a considerable amount of recent landslide sediment is still present on hillslopes, or in colluvial portions of the landscape, ready to be delivered to the fluvial system.

Sediment mixing model assumptions

In our sediment-mixing model, the initial surface N^{10}Be was calculated assuming a theoretical steady-state N^{10}Be at the Earth's surface before 2001. The model removed the N^{10}Be of material to the depths of pre-2001 landslides, implicitly assuming that recurrence times of landslides which we could not map from the 2001 Landsat image were long enough that the material had reached secular equilibrium at the background erosion rate (E_b). The timescales for reaching the equilibrium for the basins were shown in Table 3, and it seems that the assumption is unlikely to be valid, given that the returned period of an extreme event like Morakot is about 200 years (Lin et al., 2011). However, a

573 simple test with up to 20% decreases in \bar{N}_b and \bar{N}_{ls} in the model of the DN
 574 basin (E7) shows that underestimating initial $N^{10}\text{Be}$ at the surface would not
 575 have significant effects in the estimated range of E_b (Table S3). A decrease in
 576 \bar{N}_b results in an increase on the lower limit of E_b , whereas a decrease in \bar{N}_{ls}
 577 results in a decrease on the lower limit of E_b as the curvature of E_{mix} curves
 578 increase when \bar{N}_{ls} decreases in a model, leading to lower E_b at high F_{ls} . The
 579 test also shows that if the difference between the decreases in \bar{N}_b and the
 580 decreases in \bar{N}_{ls} is small, the result would be similar to the original model. The
 581 removal of the landslide material prior to 2001 in the model might result in
 582 lower surface $N^{10}\text{Be}$ at some locations as we assumed that all mapped
 583 landslides occurred in 2001. Therefore, the buildup of $N^{10}\text{Be}$ from the
 584 occurrences of landslides to 2001 was neglected. However, as the natural
 585 revegetation rate in Taiwan is high, the mapped landslides are likely <10 yr old
 586 (Hovius et al., 2000), and thus the neglected accumulation of $N^{10}\text{Be}$ should be
 587 small.

588 We also did not incorporate grain size dependence in the model, and we
 589 assumed that sand (the grain size we sampled) was produced equally from all
 590 depths in a landslide. Although it has been shown in many places that coarser
 591 sediments yield lower $N^{10}\text{Be}$ than finer sediments (Aguilar et al., 2013;
 592 Belmont et al., 2007; e.g. Brown et al., 1995; Puchol et al., 2014), there are
 593 places showing an opposite trend or no grain size dependence (Norton et al.,
 594 2008; Ouimet et al., 2009; Palumbo et al., 2010; e.g. Wittmann et al., 2007).
 595 Unfortunately, no coarse sediments are available for testing this effect in this
 596 study. As grain size distributions are likely to coarsen with depth, the
 597 abundance of sand might decrease with depth (Puchol et al., 2014; Tofelde et

al., 2018). If the majority of landslide sediments in our sand samples were from the shallower part of landslides, where $N^{10}\text{Be}$ was higher compared to that of the deeper part, the \bar{N}_{ls} would be higher than the value calculated in our model. A simple test for this case in the DN basin (E7) shows that increases in \bar{N}_{ls} would result in higher values of the lower limit of E_b compared to the original model (Table S3).

We used a spatially uniform background erosion for each basin, which may not be representative of ^{10}Be production at all places in a basin as it has been shown that uplift rate might be higher towards the main divide in the southern Central Range (Chen and Willett, 2016). In addition, landslides tend to occur close to the headwaters (Fig. 1A). Although the ^{10}Be production rate increases as elevation increases, without considering the higher erosion rates near the headwaters, we may have overestimated the mean $N^{10}\text{Be}$. However, this is not likely to affect our results too much as shown above with the simple test (Table S3).

In addition, \bar{N}_{ls} is dependent on the mean $N^{10}\text{Be}$ of all individual landslides (N_{ls}) that occurred during a time interval of 5 to 6 years, which implicitly assumes that each individual landslide supplied an amount of sediment proportional to its size. Furthermore, we assumed that at the point of sampling this sediment was well mixed with sediment supplied from other landslides and hillslopes eroded at E_b . In this scenario, sediment supply from each individual landslide only depends on the size of the landslide regardless of its timing and location. Under these assumptions, the estimated \bar{N}_{ls} might not be representative as the removal of landslide sediments over time was more complicated, and would depend on the history of channel flow conditions

at the point of sediment supply and the connectivity between the landslide and the fluvial system (Hovius et al., 2000). We tested the effect of connectivity by only using the landslides that were connected to the fluvial system (as determined from the lowest points of landslides with drainage areas $> 1 \text{ km}^2$) to calculate \bar{N}_{ls} , and the results show that the lower limit of E_b becomes slightly lower in some basins, but the upper limit remains the same (light orange bars in Fig. 5). However, even if the landslides were not connected to the fluvial system at the time when the satellite images were captured, landslide sediments could still be transported into the fluvial system by subsequent rainfall events (Li et al., 2016). Thus, the differences in the two models (i.e., one considering connectivity, and the other not) might be smaller than those shown in Fig. 5 (orange and light orange bars).

Spatial pattern of estimated background denudation rates

The spatial pattern of background denudation rate is illustrated in Figure 6. We show the maximum values, which represent the case that samples contain no recent landslide event associated landslide sediments ($F_{ls}=0$). We expect that these maximum values are higher than longer-timescale erosion rates for basins CP (E6), TML (E5), CL (E4), DC (E3), and AL (W6) because samples from these basins are likely to have higher F_{ls} given that mapped LAD is always high (Fig. 1A). Therefore, the upper limits of E_b should include landslide material in these basins, and the true E_b values should tend to the lower limits. The spatial pattern of E_b shows a northward increasing trend and shows higher values in basins east of the divide. The northward trend is reduced, if we consider lower values of E_b for basins CP (E6), TML (E5), CL

(E4), DC (E3) and AL (W6) to exclude possible landslide erosion. In any case, the rates are relatively low compared to those of basins in central Taiwan (Derrieux et al., 2014; Fellin et al., 2017), likely reflecting the early-collisional stage of the orogen in the southern part of the island.

There seems to be an abrupt increase in E_b at about 55 km N (with reference to the south tip of the island). The rate increases from 0.07 mm/yr in the SM basin (W3) to 0.80 mm/yr in the LiL basin (W4) on the west side of the divide, whereas on the eastern flank, the rate increases from 0.34 mm/yr in the DW basin (E2) to 1.67 mm/yr in the DC basin (E3) (Table 3). This boundary is coincident with the southern extent of the transition zone where the trend of the mountain range changes progressively from NNE-SSW north of this zone to N-S to the south. The abrupt change in denudation rate likely reflects the difference in the degree of collision associated with the transpression resulting from the oblique convergence of the fore-arc basin on the Philippine Sea Plate as proposed by Chang et al. (2009) on the basis of paleostress analysis. According to their “spine-like-bending” model, compression was concentrated on the eastern side of the island, which is consistent with our results that eastern basins show higher E_b than western basins. The southern extent of this concentrated compression zone seems to be along the 55 km boundary as E_b drops substantially to the south (Fig. 6). The cross-divide difference in E_b to the south is likely to be the response of the west to east tectonic advection resulting from frontal accretion, which drives material from west to east with respect to the erosional baselevel which is fixed to the coasts. The effect of this advection is to drive higher erosion rates in the east-draining basins relative to the west-draining basins (Willett et al., 2001).

We also compared E_b to the mean basin channel steepness derived from the radial χ plot method of Chen and Willett (2016) (Fig. 5). The radial χ steepness (RCS) was estimated by examining and excluding transient features associated with changes in basin channel geometry, and thus is more representative of mean basin steepness driven by the long-term tectonic uplift rate than the arithmetic mean of local steepness in a basin. We converted the RCS to erosion rate with a mean erodibility of 10^{-5} m/yr, and found that the correlation between E_b and RCS is good in basins to the north of the aforementioned boundary (55 km N), whereas to the south, E_b is systematic lower than the rate derived from RCS. This implies the relationship between E_b and RCS is not linear. The mismatch may reflect the fact that river incision outpaces hillslope processes in the south, and the valley relief is increasing as the orogen is developing (Yanites et al., 2018).

Conclusions

Repeated ^{10}Be measurements of river sediments collected from basins in the southern Central Range of Taiwan over the last decade reveal temporal variations in denudation rate in response to typhoon Morakot, presumably reflecting sediment added from storm triggered landslides. Most, though not all, basins have ^{10}Be concentrations that show an increase in erosion rate between 2006 and 2012, bracketing Morakot in time. The post-Morakot values can be up to three times higher than the lowest rates derived in the same basins, implying transient landslide-derived sediments still remained in the drainage basins after 3 years. This result demonstrates that a single ^{10}Be measurement from a sample collected following a large event in a

landslide-dominated basin can deviate significantly from the long-term denudation rate, even if the basin is regarded as large ($\sim 100 \text{ km}^2$) (Niemi et al., 2005; Yanites et al., 2009). Moreover, our results show that this perturbation can last for several years, reinforcing the importance of assessing the impact of recent mass wasting events on N^{10}Be when deriving erosion rates through cosmogenic nuclides in landslide-dominated basins. With a sediment-mixing model based on the mean basin ^{10}Be production rate, a range of background denudation rates, and estimates of the depth scaling of mapped landslides, we were able to use ^{10}Be data collected at multiple times to constrain the range of the background denudation rates for each basin and to gain some insights into changes in delivery of landslide sediment with time. The spatial pattern of background denudation rate shows a northward increase in rate from 0.06 to 1.05 mm/yr, which is three to four times lower than erosion rates found in central Taiwan, likely reflecting the early collision stage of the orogen in the south. East-draining basins exhibit higher erosion rates than west-draining basins, consistent with frontal accretion into the west verging wedge, eastward advection of rock and westward migration of the main water divide in response to rock advection of topography. Samples collected in 2015/2016 contained higher N^{10}Be than samples collected in 2012, suggesting that the delivery of landslide sediment may have decreased by this time. However, it is unclear whether this decrease in the fraction of landslide sediment is due to a decrease in the available landslide material (supply-limitation) or a lower stream transport capacity (transport-limitation) as it was relatively dry in 2014-2015. Future ^{10}Be samples can be measured to track the removal of the landslide sediments, and to continue testing the rate of decrease of sediment

removal.

724

Acknowledgements: We gratefully thank Christoph Schnabel, Cassie Fenton and Ángel Rodés for advice and support regarding the ^{10}Be cosmogenic measurements at the NERC Cosmogenic Isotope Analysis Facility, where analyses were supported by project 9025.0406. Also, we thank Negar Haghipour for her valuable guidance during ^{10}Be sample preparations, Maarten Lupker for discussions and suggestions about ^{10}Be denudation rate calculations, and everyone who helped in the field for sample collections. Thanks also to Odin Mac for discussions about landslide analysis and René Mania for elaborate landslide mapping. We thank two anonymous reviewers and the Associate Editor for helpful and constructive reviews. We acknowledge support from the Taiwan Typhoon and Flood Research Institute, National Applied Research Laboratories to provide Data Bank for Atmospheric & Hydrologic Research service. This study is supported by the Swiss National Science Foundation.

739

References

- Aguilar G, Carretier S, Regard V, Vassallo R, Riquelme R, Martinod J. 2013. Grain size-dependent ^{10}Be concentrations in alluvial stream sediment of the Huasco Valley, a semi-arid Andes region. *Quaternary Geochronology* **19** : 163–172. DOI: 10.1016/j.quageo.2013.01.011
- Belmont P, Pazzaglia FJ, Pazzaglia FJ, Gosse JC. 2007. Cosmogenic ^{10}Be as a tracer for hillslope and channel sediment dynamics in the Clearwater River, western Washington State. *Earth and Planetary Science Letters* **264** : 123–135. DOI: 10.1016/j.epsl.2007.09.013
- Bierman P, Steig EJ. 1996. Estimating rates of denudation using cosmogenic isotope abundances in sediment. *Earth Surface Processes and Landforms* **21** : 125–139.

- 752 Borchers B, Marrero S, Balco G, Caffee M, Goehring B, Lifton N, Nishiizumi K,
753 Phillips F, Schaefer J, Stone J. 2015. Geological calibration of spallation
754 production rates in the CRONUS-Earth project. *Quaternary Geochronology* **31** :
755 1–11. DOI: 10.1016/j.quageo.2015.01.009
- 756 Braucher R, Merchel S, Borgomano J, Bourlès DL. 2011. Production of
757 cosmogenic radionuclides at great depth: A multi element approach. *Earth and*
758 *Planetary Science Letters* **309** : 1–9. DOI: 10.1016/j.epsl.2011.06.036
- 759 Brown ET, Stallard RF, Larsen MC, Raisbeck GM, Yiou F. 1995. Denudation
760 rates determined from the accumulation of in situ-produced ^{10}Be in the luquillo
761 experimental forest, Puerto Rico. *Earth and Planetary Science Letters* **129** :
762 193–202. DOI: 10.1016/0012-821X(94)00249-X
- 763 Chai BHT. 1972. Structure and tectonic evolution of Taiwan. *American Journal*
764 *of Science* **272** : 389–422. DOI: 10.2475/ajs.272.5.389
- 765 Chang C-P, Angelier J, Lu C-Y. 2009. Polyphase deformation in a newly
766 emerged accretionary prism: Folding, faulting and rotation in the southern
767 Taiwan mountain range. *Tectonophysics* **466** : 395–408. DOI:
768 10.1016/j.tecto.2007.11.002
- 769 Chen C-Y, Willett SD. 2016. Graphical methods of river profile analysis to
770 unravel drainage area change, uplift and erodibility contrasts in the Central
771 Range of Taiwan. *Earth Surface Processes and Landforms* **41** : 2223–2238.
772 DOI: 10.1002/esp.3986
- 773 Chmeleff J, Blanckenburg von F, Kossert K, Jakob D. 2010. Determination of
774 the ^{10}Be half-life by multicollector ICP-MS and liquid scintillation counting.
775 *Nuclear Instruments and Methods in Physics Research Section B: Beam*
776 *Interactions with Materials and Atoms* **268** : 192–199. DOI:
777 10.1016/j.nimb.2009.09.012
- 778 Christl M, Vockenhuber C, Kubik PW, Wacker L, Lachner J, Alifimov V, Synal
779 HA. 2013. The ETH Zurich AMS facilities: Performance parameters and
780 reference materials. *Nuclear Instruments and Methods in Physics Research*
781 *Section B: Beam Interactions with Materials and Atoms* **294** : 29–38. DOI:
782 10.1016/j.nimb.2012.03.004
- 783 Dadson SJ et al. 2004. Earthquake-triggered increase in sediment delivery
784 from an active mountain belt. *Geology* **32** : 733–736. DOI: 10.1130/G20639.1
- 785 Derriex F, Siame LL, Bourlès DL, Chen R-F, Braucher R, Léanni L, Lee J-C,
786 Chu H-T, Byrne TB. 2014. How fast is the denudation of the Taiwan mountain
787 belt? Perspectives from in situ cosmogenic ^{10}Be . *Journal of Asian Earth*
788 *Sciences* **88** : 230–245. DOI: 10.1016/j.jseaes.2014.03.012
- 789 Dunai TJ. 2010. Cosmogenic Nuclides: Principles, concepts and applications
790 in the Earth surface sciences. Cambridge University Press: Cambridge

- 791 Dunne J, Elmore D, Muzikar P. 1999. Scaling factors for the rates of
792 production of cosmogenic nuclides for geometric shielding and attenuation at
793 depth on sloped surfaces. *Geomorphology* **27** : 3–11.
- 794 Fellin MG, Chen C-Y, Willett SD, Christl M, Chen Y-G. 2017. Erosion rates
795 across space and timescales from a multi-proxy study of rivers of eastern
796 Taiwan. *Global and Planetary Change* **157** : 174–193. DOI:
797 10.1016/j.gloplacha.2017.07.012
- 798 Giletycz S, Loget N, Chang C-P, Mouthereau F. 2015. Transient fluvial
799 landscape and preservation of low-relief terrains in an emerging orogen:
800 Example from Hengchun Peninsula, Taiwan. *Geomorphology* **231** : 169–181.
801 DOI: 10.1016/j.geomorph.2014.11.026
- 802 Granger DE, Kirchner JW, Finkel R. 1996. Spatially Averaged Long-Term
803 Erosion Rates Measured from in Situ-Produced Cosmogenic Nuclides in
804 Alluvial Sediment. *The Journal of Geology* **104** : 249–257.
- 805 Granger DE, Lifton NA, Willenbring JK. 2013. A cosmic trip: 25 years of
806 cosmogenic nuclides in geology. *Geological Society of America Bulletin* **125** :
807 1379–1402. DOI: 10.1130/B30774.1
- 808 Ho CS. 1986. A synthesis of the geologic evolution of Taiwan. *Tectonophysics*
809 **125** : 1–16. DOI: 10.1016/0040-1951(86)90004-1
- 810 Hovius N, Meunier P, Ching-Weei L, Hongey C, Yue-Gau C, Dadson S,
811 Ming-Jame H, Lines M. 2011. Prolonged seismically induced erosion and the
812 mass balance of a large earthquake. *Earth and Planetary Science Letters* **304** :
813 347–355. DOI: 10.1016/j.epsl.2011.02.005
- 814 Hovius N, Stark CP, Hao Tsu C, Jiun Chuan L. 2000. Supply and Removal of
815 Sediment in a Landslide-Dominated Mountain Belt: Central Range, Taiwan.
816 *The Journal of Geology* **108** : 73–89. DOI: 10.1086/314387
- 817 Howarth JD, Fitzsimons SJ, Norris RJ, Jacobsen GE. 2012. Lake sediments
818 record cycles of sediment flux driven by large earthquakes on the Alpine fault,
819 New Zealand. *Geology* **40** : 1091–1094. DOI: 10.1130/G33486.1
- 820 Huang MYF, Montgomery DR. 2013. Altered regional sediment transport
821 regime after a large typhoon, southern Taiwan. *Geology* **41** : 1223–1226. DOI:
822 10.1130/G34826.1
- 823 Ivy-Ochs S. 1996. The dating of rock surfaces using in situ produced ^{10}Be ,
824 ^{26}Al and ^{36}Cl , with examples from Antarctica and the Swiss Alps, ETH
825 dissertation
- 826 Kirby E, Whipple KX. 2012. Expression of active tectonics in erosional
827 landscapes. *Journal of Structural Geology* **44** : 54–75. DOI:
828 10.1016/j.jsg.2012.07.009

- 829 Kober F, Hippe K, Salcher B, Ivy-Ochs S, Kubik PW, Wacker L, Hählen N.
830 2012. Debris-flow-dependent variation of cosmogenically derived
831 catchment-wide denudation rates. *Geology* **40** : 935–938. DOI:
832 10.1130/G33406.1
- 833 Korschinek G, Bergmaier A, Faestermann T, Gerstmann UC, Knie K, Rugel G,
834 Wallner A, Dillmann I, Dollinger G, Gostomski von CL. 2010. A new value for
835 the half-life of ^{10}Be by Heavy-Ion Elastic Recoil Detection and liquid
836 scintillation counting. *Nuclear Instruments and Methods in Physics Research*
837 *Section B: Beam Interactions with Materials and Atoms* **268** : 187–191. DOI:
838 10.1016/j.nimb.2009.09.020
- 839 Kubik PW, Christl M. 2010. ^{10}Be and ^{26}Al measurements at the Zurich 6MV
840 Tandem AMS facility. *Nuclear Instruments and Methods in Physics Research*
841 *Section B: Beam Interactions with Materials and Atoms* **268** : 880–883. DOI:
842 10.1016/j.nimb.2009.10.054
- 843 Larsen IJ, Montgomery DR, Korup O. 2010. Landslide erosion controlled by
844 hillslope material. **3** : 247–251. DOI: 10.1038/ngeo776
- 845 Li G, West AJ, Densmore AL, Hammond DE, Jin Z, Zhang F, Wang J, Hilton
846 RG. 2016. Connectivity of earthquake-triggered landslides with the fluvial
847 network: Implications for landslide sediment transport after the 2008
848 Wenchuan earthquake. *Journal of Geophysical Research: Earth Surface* **121** :
849 703–724. DOI: 10.1002/2015JF003718
- 850 Lin C-W, Chang W-S, Liu S-H, Tsai T-T, Lee S-P, Tsang Y-C, Shieh C-L,
851 Tseng C-M. 2011. Landslides triggered by the 7 August 2009 Typhoon
852 Morakot in southern Taiwan. *Engineering Geology* **123** : 3–12. DOI:
853 10.1016/j.enggeo.2011.06.007
- 854 Malamud BD, Turcotte DL, Guzzetti F, Reichenbach P. 2004. Landslide
855 inventories and their statistical properties. *Earth Surface Processes and*
856 *Landforms* **29** : 687–711. DOI: 10.1002/esp.1064
- 857 Marc O, Hovius N. 2015. Amalgamation in landslide maps: effects and
858 automatic detection. *Natural Hazards and Earth System Sciences* **15** : 723–
859 733. DOI: 10.5194/nhess-15-723-2015
- 860 Marc O, Hovius N, Meunier P, Uchida T, Hayashi S. 2015. Transient changes
861 of landslide rates after earthquakes. *Geology* **43** : 883–886. DOI:
862 10.1130/G36961.1
- 863 Müller AM, Christl M, Lachner J, Suter M, Synal HA. 2010. Competitive ^{10}Be
864 measurements below 1MeV with the upgraded ETH–TANDY AMS facility.
865 *Nuclear Instruments and Methods in Physics Research Section B: Beam*
866 *Interactions with Materials and Atoms* **268** : 2801–2807. DOI:
867 10.1016/j.nimb.2010.05.104

- 868 Niemi NA, Oskin M, Burbank DW, Heimsath AM, Gabet EJ. 2005. Effects of
869 bedrock landslides on cosmogenically determined erosion rates. *Earth and*
870 *Planetary Science Letters* **237** : 480–498. DOI: 10.1016/j.epsl.2005.07.009
- 871 Nishiizumi K, Imamura M, Caffee MW, Southon JR, Finkel RC, McAninch J.
872 2007. Absolute calibration of ^{10}Be AMS standards. *Nuclear Instruments and*
873 *Methods in Physics Research Section B: Beam Interactions with Materials and*
874 *Atoms* **258** : 403–413. DOI: 10.1016/j.nimb.2007.01.297
- 875 Norton KP, Blanckenburg von F, Schlunegger F, Schwab M, Kubik PW. 2008.
876 Cosmogenic nuclide-based investigation of spatial erosion and hillslope
877 channel coupling in the transient foreland of the Swiss Alps. *Geomorphology*
878 **95** : 474–486. DOI: 10.1016/j.geomorph.2007.07.013
- 879 Ouimet WB, Whipple KX, Granger DE. 2009. Beyond threshold hillslopes:
880 Channel adjustment to base-level fall in tectonically active mountain ranges.
881 *Geology* **37** : 579–582. DOI: 10.1130/G30013A.1
- 882 Palumbo L, Hetzel R, Tao M, Li X. 2010. Topographic and lithologic control on
883 catchment-wide denudation rates derived from cosmogenic ^{10}Be in two
884 mountain ranges at the margin of NE Tibet. *Geomorphology* **117** : 130–142.
885 DOI: 10.1016/j.geomorph.2009.11.019
- 886 Portenga EW, Bierman PR. 2011. Understanding Earth's eroding surface with
887 ^{10}Be . **21** : 4–10. DOI: 10.1130/G111A.1
- 888 Puchol N, Lavé J, Lupker M, Blard P-H, Gallo F, France-Lanord C. 2014.
889 Grain-size dependent concentration of cosmogenic ^{10}Be and erosion
890 dynamics in a landslide-dominated Himalayan watershed. *Geomorphology*
891 **224** : 55–68. DOI: 10.1016/j.geomorph.2014.06.019
- 892 Reiners PW, Brandon MT. 2006. Using thermochronology to understand
893 orogenic erosion. *Annual Review of Earth and Planetary Sciences* **34** : 419–
894 466.
- 895 Schwanghart W, Scherler D. 2014. Short Communication: TopoToolbox 2 –
896 MATLAB-based software for topographic analysis and modeling in Earth
897 surface sciences. *Earth Surface Dynamics* **2** : 1–7. DOI:
898 10.5194/esurf-2-1-2014
- 899 Sosa Gonzalez V, Schmidt AH, Bierman PR, Rood DH. 2017. Spatial and
900 temporal replicability of meteoric and in situ ^{10}Be concentrations in fluvial
901 sediment. *Earth Surface Processes and Landforms* **42** : 2570–2584. DOI:
902 10.1002/esp.4205
- 903 Stone JO. 2000. Air pressure and cosmogenic isotope production. *Journal of*
904 *Geophysical Research-Solid Earth* **105** : 23753–23759.
- 905 Syvitski JPM, Milliman JD. 2007. Geology, Geography, and Humans Battle for
906 Dominance over the Delivery of Fluvial Sediment to the Coastal Ocean. *The*
907 *Journal of Geology* **115** : 1–19. DOI: 10.1086/509246

- 908 Tofelde S, Duesing W, Schildgen TF, Wickert AD, Wittmann H, Alonso RN,
909 Strecker M. 2018. Effects of deep-seated versus shallow hillslope processes
910 on cosmogenic ^{10}Be concentrations in fluvial sand and gravel. *Earth Surface
911 Processes and Landforms* **43** : 3086–3098. DOI: 10.1002/esp.4471
- 912 Wang J, Jin Z, Hilton RG, Zhang F, Densmore AL, Li G, West AJ. 2015.
913 Controls on fluvial evacuation of sediment from earthquake-triggered
914 landslides. *Geology* **43** : 115–118. DOI: 10.1130/G36157.1
- 915 Ward GK, Wilson SR. 1978. Procedures for comparing and combining
916 radiocarbon age determinations: a critique. *Archaeometry* **20** : 19–31.
- 917 West AJ, Li G, Zhang F, Hilton RG, Densmore AL. 2014. Dilution of ^{10}Be in
918 detrital quartz by earthquake-induced landslides: Implications for determining
919 denudation rates and potential to provide insights into landslide sediment
920 dynamics. *Earth and Planetary Science Letters* **396** : 143–153. DOI:
921 10.1016/j.epsl.2014.03.058
- 922 West AJ, Lin CW, Lin TC, Hilton RG, Liu SH, Chang CT, Lin KC, Galy A,
923 Sparkes RB, Hovius N. 2011. Mobilization and transport of coarse woody
924 debris to the oceans triggered by an extreme tropical storm. *Limnology and
925 Oceanography* **56** : 77–85. DOI: 10.4319/lo.2011.56.1.0077
- 926 Willett SD, Slingerland R, Hovius N. 2001. Uplift, shortening, and steady state
927 topography in active mountain belts. *American Journal of Science* **301** : 455–
928 485.
- 929 Wittmann H, Blanckenburg von F, Kruesmann T, Norton KP, Kubik PW. 2007.
930 Relation between rock uplift and denudation from cosmogenic nuclides in river
931 sediment in the Central Alps of Switzerland. *Journal of Geophysical Research:
932 Solid Earth (1978–2012)* **112** : F04010. DOI: 10.1029/2006JF000729
- 933 Yanites BJ, Mitchell NA, Bregy JC, Carlson GA, Cataldo K, Holahan M,
934 Johnston GH, Nelson A, Valenza J, Wanker M. 2018. Landslides control the
935 spatial and temporal variation of channel width in southern Taiwan:
936 Implications for landscape evolution and cascading hazards in steep,
937 tectonically active landscapes. *Earth Surface Processes and Landforms* **43** :
938 1782–1797. DOI: 10.1002/esp.4353
- 939 Yanites BJ, Tucker GE, Anderson RS. 2009. Numerical and analytical models
940 of cosmogenic radionuclide dynamics in landslide-dominated drainage basins.
941 *Journal of Geophysical Research* **114** : F01007. DOI: 10.1029/2008JF001088
- 942 Yu S-B, Chen H-Y, Kuo L-C. 1997. Velocity field of GPS stations in the Taiwan
943 area. *Tectonophysics* **274** : 41–59.

944

Figure Captions

Fig. 1 The study site in southern Taiwan. (A) Landslides that occurred during four time periods (2001-2006, 2007-2009, 2010-2012 and 2013-2014) in the southern Central Range. White lines show boundaries of studied drainage basins. Abbreviations of basin names are shown near outlets of basins. Inset shows the tectonic framework of Taiwan. The black arrow indicates the current direction and velocity of the Philippine Sea Plate relative to the Eurasia Plate obtained from GPS measurements (Yu et al., 1997). (B) Geologic map showing lithology of the study area from the Central Geological Survey of Taiwan. Detrital ^{10}Be sample sites are shown with red circles and sample names are marked close to the circles. Black solid lines depict the upstream drainage boundaries of ^{10}Be sample sites.

Fig. 2 Normalized ^{10}Be -based denudation rate, annual precipitation, and landslide areal density as a function of time since 2005. Results are shown for individual drainage basins with locations in Figure 1. Normalized ^{10}Be is defined as the ^{10}Be -derived rate, divided by the minimum measured denudation rate in each basin and is represented by the red circles with error bars. The areal density of new landslides (as %) is shown by light grey boxes, and annual precipitation integrated over each basin, expressed in meter, is shown by a fine blue line. Plots are arranged according to geographic locations of basins, permitting regional comparison.

Fig. 3 The relationship between the measured ^{10}Be concentration (C) and the areal density of landslides (LAD). The ^{10}Be concentration in 2006, 2012, and

2015/2016 was compared to the LAD over the periods of 2001-2006, 2007-2012, and 2010/2014, respectively. We also compared the ^{10}Be concentration to the areal density of shallow (LAD_s) and deep (LAD_d) landslides classified by the landslide size of 10^5 m^2 . The black, blue and red lines and texts show the results of regression with all data, all data except data of basins SM, FS, and FK, and all data except basins LP, LiL, SM, FS, and FK, respectively. Correlation coefficients of the regressions are shown in Table S1.

Fig. 4 The relationship between the normalized changes in measured ^{10}Be concentration and normalized changes in scar area and volume of landslides over the periods of 2006-2012 and 2006-2015/2016. We also compared the normalized changes in N^{10}Be to normalized changes in scar area and volume of shallow and deep landslides classified by the landslide size of 10^5 m^2 . Correlation coefficients of the regressions are shown in Table S2.

Fig. 5 Comparison of cosmogenic-derived denudation rates with rates inferred from mean basin steepness. The data shown on the left and right sides of 0 represent west and east flowing basins, respectively. Mean basin steepness data (black diamonds) are radial χ plot fits (RCS) from Chen and Willett (2016), and were converted to erosion rate with a mean erodibility of 10^{-5} m/yr . Denudation rates derived from ^{10}Be samples are shown with green, red and blue circles and error bars for samples collected in 2006, 2012 and 2015/2016, respectively. Ranges of estimated background denudation rates estimated by sediment-mixing models are shown with orange bars.

Fig. 6 The pattern of maximum background denudation rate estimated from the sediment-mixing model, representing the case of no landslide sediment dilution in ^{10}Be samples. The blue solid dash line at 55 km N from the south tip of the island shows the boundary of abrupt changes in denudation rate.

For Peer Review

1
2
3
4
5
6
7
8
9
10
11
12
13
14
15
16
17
18
19
20
21
22
23
24
25
26
27
28
29
30
31
32
33
34
35
36
37
38
39
40
41
42
43
44
45
46
47
48
49
50
51
52
53
54
55
56
57
58
59
60

1000 **Tables**

1001 **Table 1** Analytical data and concentrations of ¹⁰Be in quartz from river
1002 sediment samples. Batches A-F were measured at ETH Zurich, whereas other
1003 batches were measured at SUERC.

Batch ID	Lab #	Sample #	¹⁰ Be counts	¹⁰ Be/ ⁹ Be (10 ⁻¹⁵)	uncert. (%)	χ ²	carrier (mg)	sample weight (g)	¹⁰ Be (10 ³ at/g)	uncert. (10 ³ at/g)
A	TB1960	ST11	50	92.5	15.26	35.89	0.198	96.78	11.65	1.94
	TB1961	ST13	35	18.54	21.15	6.93	0.202	88.74	1.68	0.61
	TB1962	ST14	18	13.64	23.57	3.02	0.198	94.21	0.87	0.47
	TB1963	ST16	101	45.44	10.33	59.27	0.199	98.51	5.13	0.64
	TB1967	TW12-21	33	15.25	17.41	6.48	0.198	94.74	1.09	0.39
Blank (A)	TB1968	BK01	27	7.93	19.76		0.199			
	TB1969	BK02	25	7.3	20		0.197			
	TB1970	BK03	16	6.5	25		0.197			
	TB1971	BK04	19	7.98	27.83		0.199			
	TB1972	BK05	33	8	24.48		0.194			
error weighted mean blank (A)				7.46	10.23					
B	TB1977	ST09	341	83.51	5.42	267.41	0.201	95.74	10.58	0.65
Blank (B)	TB1983	Blank1	42	7.86	15.6		0.196			
	TB1984	Blank2	33	7.95	19.09		0.195			
error weighted mean blank (B)				7.9	12.08					
C	TB2295	TW12-16	378	169.8	5.3	332.78	0.198	61.18	35.68	1.96
	TB2296	TW12-17	109	42.6	9.7	79.84	0.205	94.78	5.46	0.61
	TB2297	TW12-18	183	67.9	9.5	93.83	0.207	93.09	9.37	0.97
	TB2298	TW12-19	99	36.7	12.9	43.79	0.198	52.94	7.97	1.2
	TB2299	ST01	99	33	10.1	66.66	0.206	85.78	4.52	0.55
	TB2300	ST03	810	295.6	3.7	702.11	0.206	88.48	45.24	1.71
	TB2301	ST05	466	222.9	4.8	412.57	0.207	68.88	43.8	2.16
	TB2302	ST06	332	142.8	7	189.03	0.207	53.47	35.7	2.6
	TB2303	FK	250	109	7.5	160.49	0.208	73.12	19.8	1.56
	TB2304	SM	492	211.9	4.7	428.87	0.206	50.73	56.19	2.71
Blank (C)	TB2305	LP	54	36.4	13.7	38.86	0.206	81.36	5.35	0.86
	TB2306	BK01	14	4.2	26.8		0.203			
	TB2307	BK02	18	5.9	25.6		0.197			
error weighted mean blank (C)				4.81	18.78					
D	TB2309	ST13	28	9.1	19	8.86	0.204	88.1	0.92	0.29
	TB2310	ST14	29	13.8	23.9	9.56	0.2	95.93	1.49	0.47
Blank (D)	TB2321	Blank1	8	2.9	38.2		0.206			
	TB2322	Blank2	11	4.3	30.2		0.206			
	TB2323	Blank3	4	2.2	62		0.206			
error weighted mean blank (D)				3.13	22.88					
E	TB2574	ST13	33	16.99	17.45	7.14	0.207	98.25	1.21	0.45
	TB2575	ST14	38	11.09	16.27	1.52	0.206	99.79	0.37	0.3
Blank (E)	TB2584	BK01	35	9.3	17.5		0.206			
	TB2585	BK02	13	7.06	27.77		0.207			
error weighted mean blank (E)				8.38	14.93					
F	TB2757	TW16-01	100	24.62	13.31	23.23	0.206	101.87	2.31	0.46
	TB2758	TW16-02	39	22.31	17.08	13.34	0.207	96.83	2.11	0.56
	TB2759	TW16-03	48	20.55	14.5	15.82	0.208	96.14	1.88	0.45
	TB2760	TW16-04	130	26.59	9.83	41.99	0.206	98.49	2.66	0.39
	TB2761	TW16-05	66	25.89	13.23	24.83	0.206	97.28	2.59	0.5
	TB2762	TW16-06	120	66.69	9.22	88.3	0.207	94.89	8.62	0.91
	TB2763	TW16-07	106	20.59	9.86	28.72	0.2	96.9	1.8	0.31
	TB2765	ST14	26	26.07	19.66	12.21	0.2	100.6	2.46	0.69
Blank (F)	TB2766	BK01	18	6.27	29.29		0.207			
	TB2767	BK02	27	7.19	19.3		0.207			
	TB2768	BK03	27	9.48	19.3		0.207			
error weighted mean blank (F)				7.56	12.53					

Batch ID	Lab #	Sample #	¹⁰ Be counts	¹⁰ Be/ ⁹ Be (10 ⁻¹⁵)	uncert. (%)	χ ²	carrier (mg)	weight (g)	¹⁰ Be (10 ³ at/g)	uncert. (10 ³ at/g)
G	b2136	ST09		30.94	9.07	57.42	0.115	12.1	16.51	2.19
Blank (G)	b2141	CB2208071		7.5	17.42		0.116			
H	b2365	ST12		12.91	11.4	49.14	0.405	65.1	1.85	0.26
Blank (H)	b2366	CB150108		1.93	27.74		0.407			
I	b3276	ST02		27.8	5.67	124.57	0.111	35.9	4.29	0.66
Blank (I)	b3283	CB020309		5.04	25.72		0.204			
J	b4380	ST15		14.16	8.87	44.27	0.285	44.2	1.87	0.28
Blank (J)	b4382	CW040510		3.47	28.87		0.285			

Table 2 Summary of ^{10}Be sample locations, basin characteristics, denudation rates and integration timescales. Samples listed in italics are data from Fellin et al. (2017).

Basin #	Basin ID	Basin name	Sample #	Sampling date (dd-mm-yr)	Lon (°)	Lat (°)	Dist. to S tip ^a (km)	Basin area (km ²)	N ^b ± 1σ (10 ³ at/g)	P _n ^c	P _{ms} ^c (at/g yr)	P _{mf} ^c	Denudation rate ^d (mm/yr)	Uncertainty -34 %	+34 %	Time scale (yr)	Source ^e
Eastern basins																	
E7	DN	Danan	ST16	Mar-06	121.034	22.764	98.72	103.7	5.13 ± 0.64	6.74	0.013	0.033	0.90	0.14	0.15	662	This study
			TW12-15	3-Dec-12	121.034	22.764	98.72	103.7	1.49 ± 0.32	6.74	0.013	0.033	3.09	0.64	0.87	192	A
			TW16-01	1-Feb-16	121.030	22.764	98.82	103.6	2.31 ± 0.46	6.74	0.013	0.033	1.99	0.39	0.51	297	This study
E6	CP	Chihpen	ST15	Mar-06	121.012	22.695	90.67	160.3	1.87 ± 0.28	6.43	0.013	0.033	2.36	0.39	0.47	251	This study
			TW12-13	3-Dec-12	120.982	22.682	90.67	142.5	1.22 ± 0.34	6.70	0.013	0.034	3.75	0.90	1.56	158	A
			TW16-02	1-Feb-16	120.980	22.682	88.45	142.6	2.11 ± 0.56	6.70	0.013	0.034	2.18	0.50	0.82	272	This study
E5	TML	Taimali	ST14-WM	Mar-06	120.963	22.592	78.96	191.7	1.79 ± 0.45	6.00	0.012	0.032	2.31	0.53	0.81	257	This study
			TW12-12	2-Dec-12	120.945	22.594	78.96	182.2	1.11 ± 0.34	6.10	0.013	0.032	3.78	0.97	1.62	157	A
			TW16-03	2-Feb-16	120.960	22.595	78.46	187.0	1.88 ± 0.45	6.05	0.013	0.032	2.22	0.50	0.71	267	This study
E4	CL	Chinlun	ST13-WM	Mar-06	120.934	22.524	71.13	127.5	1.10 ± 0.23	5.88	0.012	0.032	3.69	0.72	1.03	161	This study
			TW12-11	2-Dec-12	120.943	22.530	71.13	136.5	1.02 ± 0.37	5.76	0.012	0.032	3.93	1.13	2.21	151	A
			TW16-04	1-Feb-16	120.940	22.529	71.23	136.5	2.66 ± 0.39	5.76	0.012	0.032	1.50	0.25	0.30	396	This study
E3	DC	Dachu	ST12	Mar-06	120.926	22.462	62.87	124.8	1.85 ± 0.26	4.82	0.011	0.031	1.84	0.30	0.37	321	This study
			TW12-10	2-Dec-12	120.925	22.463	62.87	124.8	1.49 ± 0.32	4.82	0.011	0.031	2.29	0.47	0.68	258	A
			TW16-05	2-Feb-16	120.930	22.463	63.71	124.8	2.59 ± 0.50	4.82	0.011	0.031	1.32	0.25	0.35	450	This study
E2	DW	Dawu	ST11	Mar-06	120.890	22.359	51.51	102.9	11.65 ± 1.94	4.46	0.011	0.030	0.27	0.05	0.07	2170	This study
			DWmean	2-Dec-12	-	-	51.58	98.6	-	-	-	-	0.96	0.14	0.18	620	A
			TW16-06	2-Feb-16	120.900	22.362	52.14	103.2	8.62 ± 0.91	4.46	0.011	0.030	0.37	0.05	0.06	1605	This study
E1	AS	Anshuo	ST09-WM	Mar-06	120.873	22.292	44.63	49.2	11.06 ± 1.61	3.65	0.010	0.029	0.24	0.04	0.05	2442	This study
			ASmean	2-Dec-12	-	-	43.44	39.5	-	-	-	-	0.33	0.04	0.04	1786	A
Western basins																	
W6	AL	Ailiao	TW12-21	4-Dec-12	120.652	22.710	79.62	408.3	1.09 ± 0.39	7.32	0.014	0.034	4.55	1.29	2.41	130	This study
			TW16-07	2-Feb-16	120.650	22.711	79.34	408.4	1.80 ± 0.31	7.32	0.014	0.034	2.76	0.48	0.64	215	This study
			ST01	Mar-06	120.657	22.527	56.23	116.9	4.52 ± 0.55	5.73	0.012	0.032	0.88	0.13	0.15	675	This study
W5	LP	Linpien	TW12-18	4-Dec-12	120.678	22.528	61.41	39.7	9.37 ± 0.97	5.85	0.012	0.032	0.43	0.06	0.06	1374	This study
			TW12-19	4-Dec-12	120.660	22.536	61.61	70.4	7.97 ± 1.20	5.85	0.012	0.032	0.51	0.08	0.11	1168	This study
			LPmean	4-Dec-12	-	-	61.51	110.1	-	-	-	-	0.48	0.06	0.07	1235	This study
W4	LIL	Lili	LP	5-Jan-15	120.656	22.526	56.23	116.9	5.35 ± 0.86	5.73	0.012	0.032	0.74	0.13	0.16	798	This study
			ST02	Mar-06	120.645	22.438	49.62	110.4	4.29 ± 0.66	5.26	0.012	0.032	0.86	0.15	0.17	687	This study
			TW12-17	3-Dec-12	120.654	22.443	51.8	108.8	5.46 ± 0.61	5.29	0.012	0.032	0.68	0.09	0.12	871	This study
W3	SM	Shuaimang	ST03	Mar-06	120.638	22.353	41.82	86.3	45.24 ± 1.71	4.50	0.011	0.030	0.07	0.01	0.01	8353	This study
			TW12-16	3-Dec-12	120.649	22.368	43.77	64.3	35.68 ± 1.96	4.66	0.011	0.031	0.09	0.01	0.02	6369	This study
			SM	5-Jan-15	120.639	22.353	41.82	86.3	56.19 ± 2.71	4.50	0.011	0.030	0.06	0.00	0.01	10375	This study
W2	FS	Fangshan	ST05	Mar-06	120.678	22.263	33.37	105.1	43.80 ± 2.16	4.30	0.011	0.030	0.07	0.01	0.01	8403	This study
			TW12-04	1-Dec-12	120.725	22.280	37.45	55.6	33.10 ± 1.44	4.78	0.011	0.031	0.10	0.01	0.02	5791	This study
			TW12-05	1-Dec-12	120.739	22.273	37.26	25.9	49.28 ± 2.44	4.08	0.010	0.030	0.06	0.00	0.01	9884	This study
W1	FK	Fengkang	FSmean	1-Dec-12	-	-	37.36	81.6	-	-	-	-	0.09	0.01	0.01	6670	This study
			ST06	Mar-06	120.727	22.211	27.46	84.6	35.70 ± 2.60	3.72	0.010	0.029	0.08	0.01	0.01	7770	This study
			FK	5-Jan-15	120.728	22.211	27.46	84.6	19.80 ± 1.56	3.61	0.010	0.029	0.13	0.02	0.02	4416	This study

^a Distance from the outlet of each basin to the southernmost tip of the island of Taiwan.

^b ^{10}Be concentration

^c Mean basin ^{10}Be production rates of neutrons (P_n), slow muons (P_{ms}) and fast muons (P_{mf}).

^d Denudation rates calculated from Eq. (1)

^e A = Fellin et al., (2017).

1
2
3
4
5
6
7
8
9
10
11
12
13
14
15
16
17
18
19
20
21
22
23
24
25
26
27
28
29
30
31
32
33
34
35
36
37
38
39
40
41
42
43
44
45
46
47
48
49
50
51
52
53
54
55
56
57
58
59
60

Table 3 Summary of landslide areal densities, mean landslide depths, ranges of background denudation rates, integration timescales, and the fraction of landslide sediment in each basin over each time period. Areal density and mean depth of landslides are shown for time periods of 2001-2006 (01-06), 2007-2012 (07-12), and 2010-2014 (10-14).

Basin #	Basin ID	Basin area (km ²)	Landslide areal density (LAD) (%) ^a			Total volume of lanslides (m ³) ^b			Mean depth of landslides (m) ^c			Background denudation rate (mm/yr) ^d		Timescale (yr) ^d		Fraction of landslide sediments ^d					
			01-06	07-12	10-14	01-06	07-12	10-14	01-06	07-12	10-14	min	max	min	max	2006		2012		2016	
Eastern basins																					
E7	DN	103.6	0.14	0.28	0.54	2.6 × 10 ⁵	5.6 × 10 ⁵	1.1 × 10 ⁶	1.6	1.7	1.7	0.78	1.05	760	564	0	0.50	0.84	1	0.51	1
E6	CP	160.3	0.27	1.17	0.53	9.2 × 10 ⁵	4.9 × 10 ⁶	1.6 × 10 ⁶	2.1	2.4	1.7	0.83	2.83	717	209	0	1	0.01	1	0	1
E5	TML	191.7	1.20	4.46	1.02	6.7 × 10 ⁶	8.8 × 10 ⁷	3.9 × 10 ⁶	2.9	11.9	1.9	0.64	2.93	923	202	0	1	0	1	0	1
E4	CL	136.5	0.67	3.40	0.42	2.6 × 10 ⁶	1.6 × 10 ⁷	1.1 × 10 ⁶	2.8	3.4	1.7	0.83	1.80	715	329	0.55	1	0.47	1	0	1
E3	DC	124.8	0.28	1.88	0.09	7.3 × 10 ⁵	1.1 × 10 ⁷	1.9 × 10 ⁵	2.0	5.1	1.5	0.56	1.67	1065	355	0	1	0.10	1	0	1
E2	DW	103.2	0.16	1.58	0.17	6.2 × 10 ⁵	1.6 × 10 ⁷	4.7 × 10 ⁵	3.8	10.8	2.3	0.10	0.34	6171	1745	0	1	0.66	1	0	1
E1	AS	49.3	0	0.23	0.03	-	3.9 × 10 ⁵	4.1 × 10 ⁴	-	3.4	3.1	0.20	0.29	2963	2043	0	0	0	0.74	-	-
Western basins																					
W6	AL	408.4	0.70	3.32	0.82	6.9 × 10 ⁶	7.7 × 10 ⁷	6.6 × 10 ⁶	2.3	6.1	1.9	0.77	3.40	767	174	-	-	0	1	0	1
W5	LP	116.9	0.09	2.95	0.22	3.3 × 10 ⁵	3.4 × 10 ⁷	1.3 × 10 ⁶	3.0	8.8	5.3	0.23	0.55	2560	1078	0.39	1	0	0.71	0.12	1
W4	LiL	110.4	0.16	2.43	0.33	3.8 × 10 ⁵	2.0 × 10 ⁷	8.8 × 10 ⁵	2.0	8.4	2.3	0.21	0.80	2792	741	0	1	0	0.92	-	-
W3	SM	86.3	0.03	0.58	0.10	5.6 × 10 ⁴	1.3 × 10 ⁶	1.4 × 10 ⁵	2.1	2.4	1.5	0.02	0.07	25647	8510	0	1	0.18	1	0	1
W2	FS	105.1	0.09	0.38	0.10	1.4 × 10 ⁵	9.8 × 10 ⁵	1.7 × 10 ⁵	1.5	2.3	1.6	0.02	0.08	24520	7442	0	1	0	1	-	-
W1	FK	84.6	0.05	0.12	0.01	7.4 × 10 ⁴	2.3 × 10 ⁵	1.1 × 10 ⁴	1.6	2.2	1.2	0.05	0.09	12207	6620	0	0.97	-	-	0.33	1

^a Areal density of landslides calculated from landslide inventories, showing the total scar area of newly detected landslides divided by basin area over each time period.

^b Total volume of landslides calculated based on area-volume scaling relationship of landslides.

^c Mean depth of mean depths of landslides calculated from Eq. (2).

^d Results obtained from the sediment-mixing model.

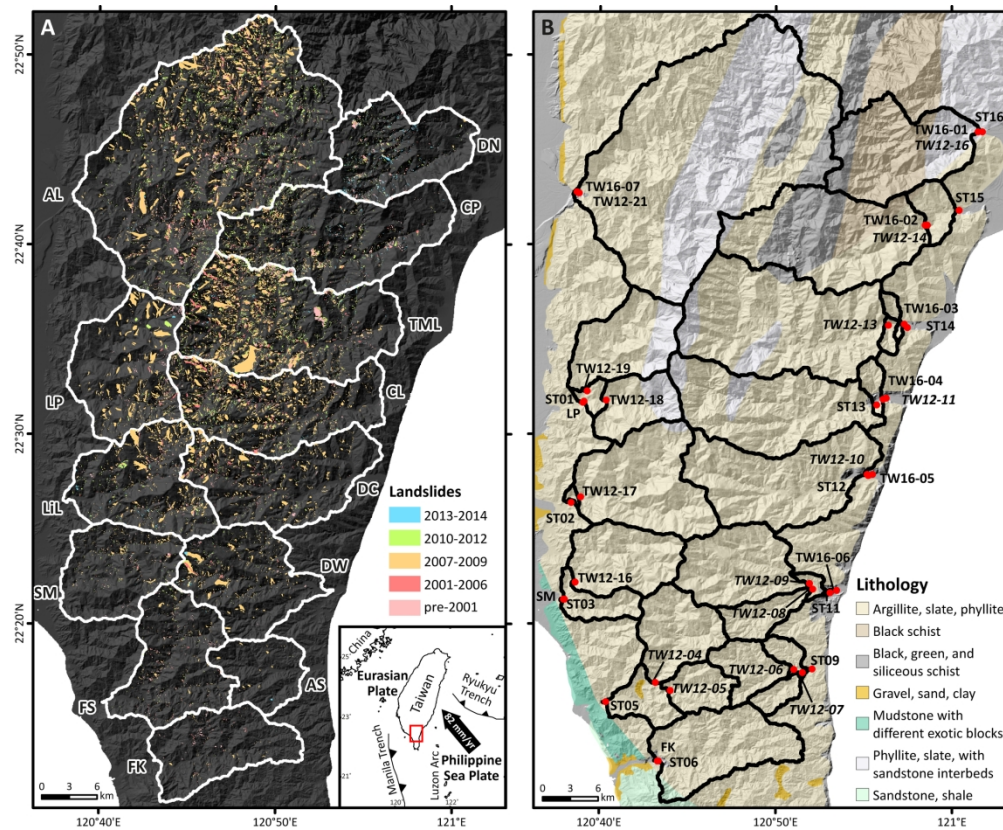


Fig. 1 The study site in southern Taiwan. (A) Landslides that occurred during four time periods (2001-2006, 2007-2009, 2010-2012 and 2013-2014) in the southern Central Range. White lines show boundaries of studied drainage basins. Abbreviations of basin names are shown near outlets of basins. Inset shows the tectonic framework of Taiwan. The black arrow indicates the current direction and velocity of the Philippine Sea Plate relative to the Eurasia Plate obtained from GPS measurements (Yu et al., 1997). (B) Geologic map showing lithology of the study area from the Central Geological Survey of Taiwan. Detrital ^{10}Be sample sites are shown with red circles and sample names are marked close to the circles. Black solid lines depict the upstream drainage boundaries of ^{10}Be sample sites.

202x167mm (300 x 300 DPI)

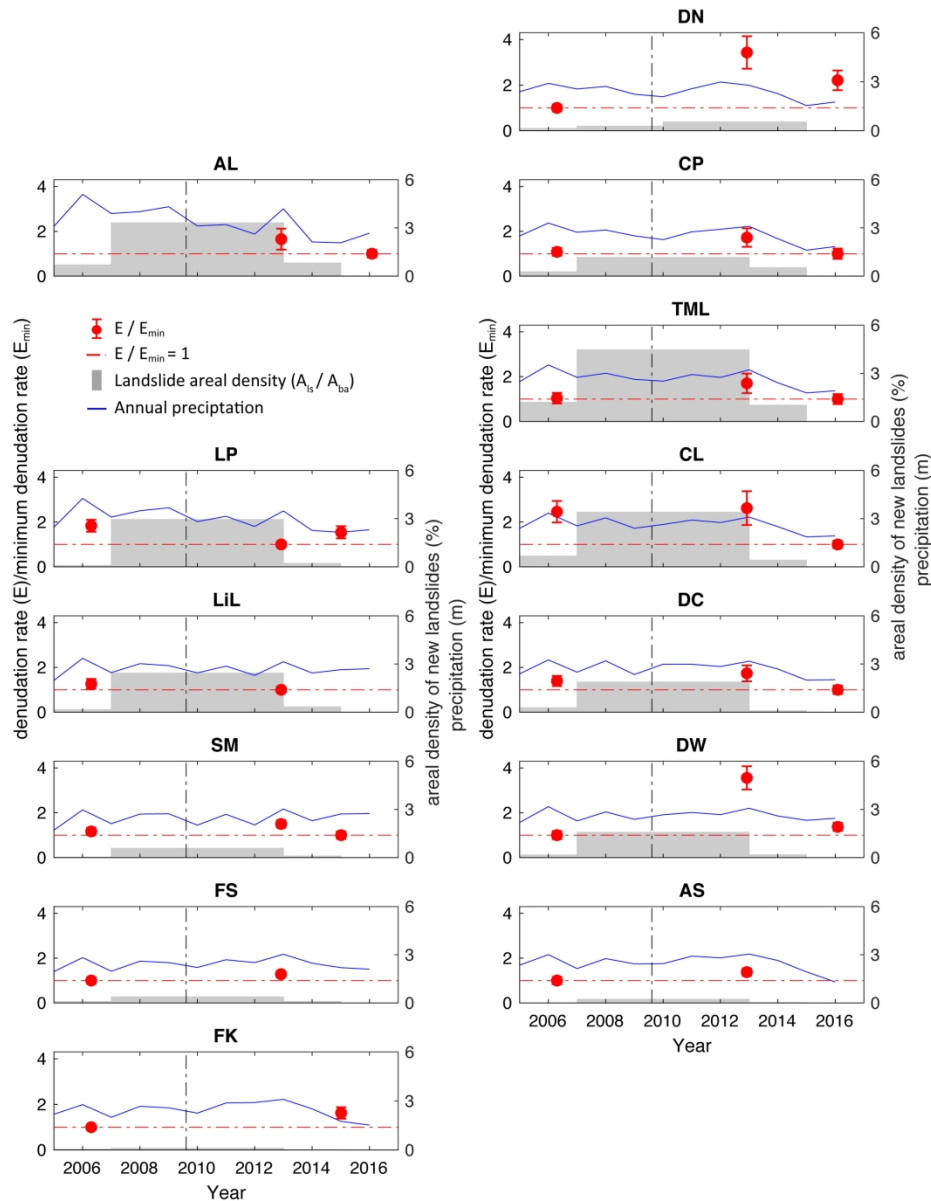
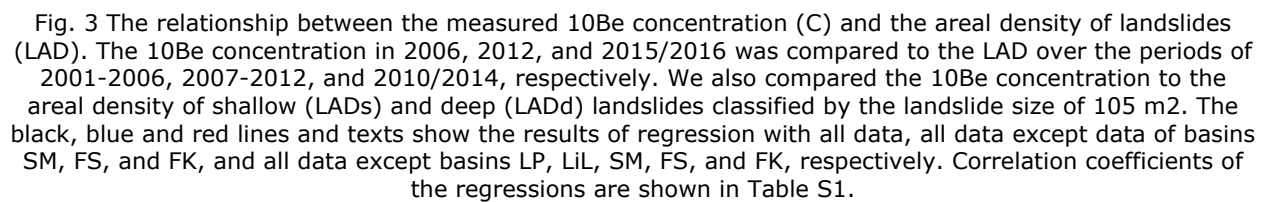


Fig. 2 Normalized ^{10}Be -based denudation rate, annual precipitation, and landslide areal density as a function of time since 2005. Results are shown for individual drainage basins with locations in Figure 1. Normalized ^{10}Be is defined as the ^{10}Be -derived rate, divided by the minimum measured denudation rate in each basin and is represented by the red circles with error bars. The areal density of new landslides (as %) is shown by light grey boxes, and annual precipitation integrated over each basin, expressed in meter, is shown by a fine blue line. Plots are arranged according to geographic locations of basins, permitting regional comparison.

193x250mm (300 x 300 DPI)



<http://mc.manuscriptcentral.com/esp>

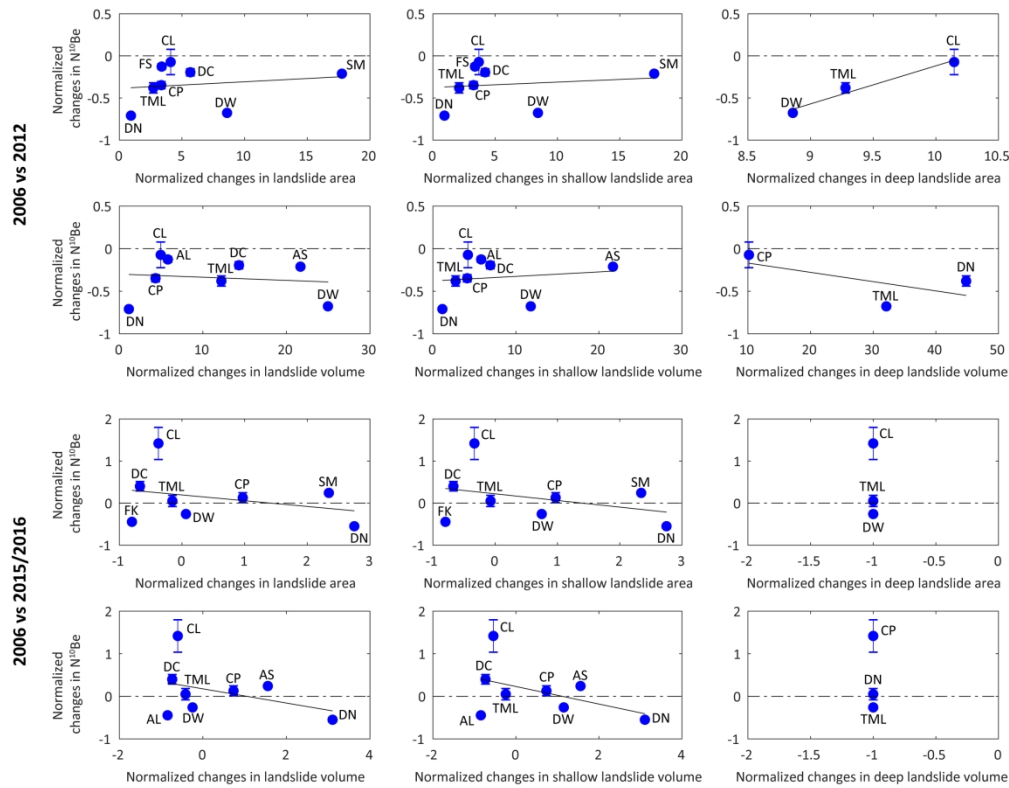


Fig. 4 The relationship between the normalized changes in measured ^{10}Be concentration and normalized changes in scar area and volume of landslides over the periods of 2006-2012 and 2006-2015/2016. We also compared the normalized changes in ^{10}Be to normalized changes in scar area and volume of shallow and deep landslides classified by the landslide size of 105 m². Correlation coefficients of the regressions are shown in Table S2.

240x187mm (300 x 300 DPI)

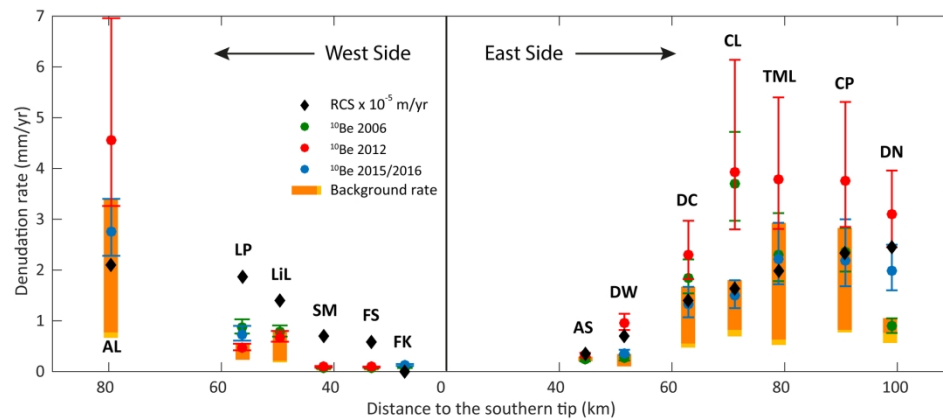


Fig. 5 Comparison of cosmogenic-derived denudation rates with rates inferred from mean basin steepness. The data shown on the left and right sides of 0 represent west and east flowing basins, respectively. Mean basin steepness data (black diamonds) are radial χ plot fits (RCS) from Chen and Willett (2016), and were converted to erosion rate with a mean erodibility of 0.01. Denudation rates derived from ¹⁰Be samples are shown with green, red and blue circles and error bars for samples collected in 2006, 2012 and 2015/2016, respectively. Ranges of estimated background denudation rates estimated by sediment-mixing models are shown with orange bars.

198x82mm (300 x 300 DPI)

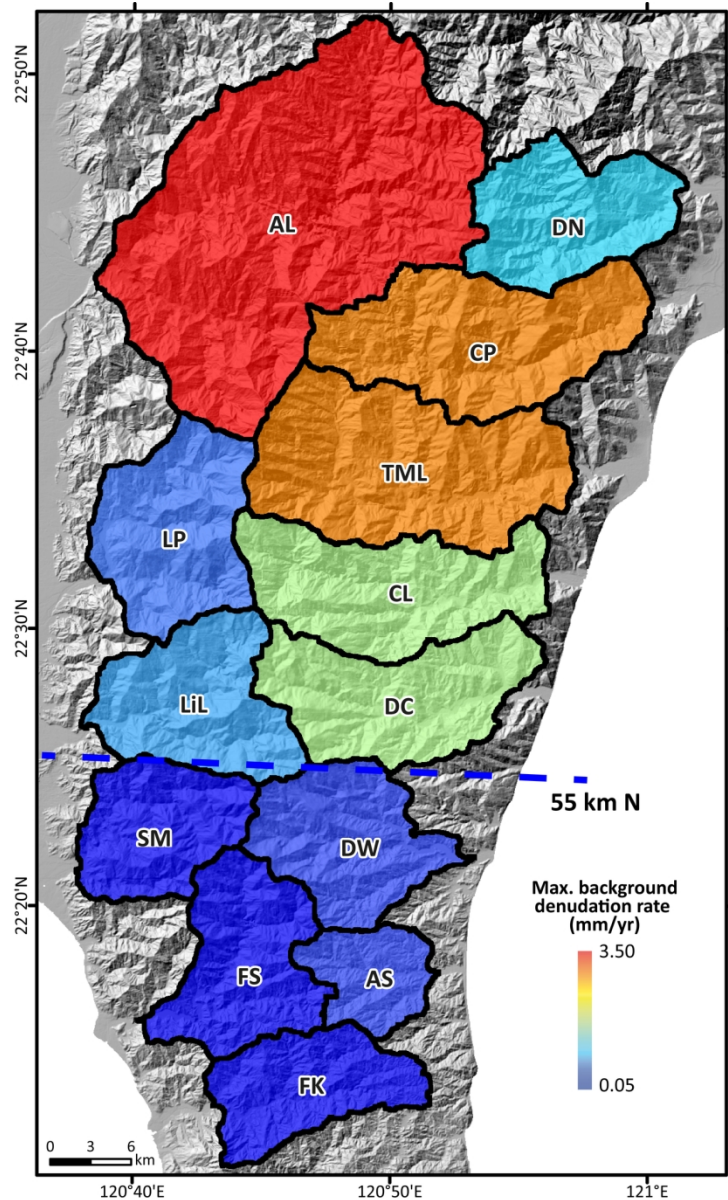


Fig. 6 The pattern of maximum background denudation rate estimated from the sediment-mixing model, representing the case of no landslide sediment dilution in 10Be samples. The blue solid dash line at 55 km N from the south tip of the island shows the boundary of abrupt changes in denudation rate.

115x191mm (300 x 300 DPI)

Supplementary Materials

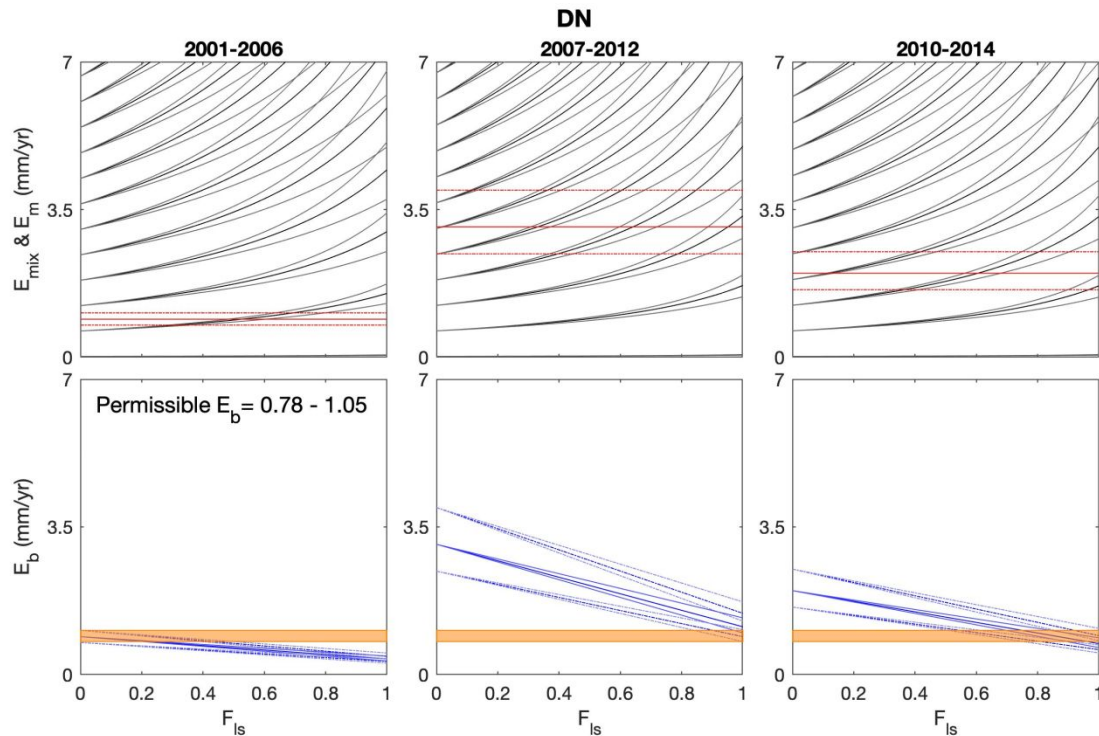


Fig. S1 Result of sediment-mixing model for the basin DN. For each time period, upper panel shows the fraction of landslide sediments (F_{ls}) versus modeled denudation rates (E_{mix} ; black and grey curves show models using d_{ls} and $d_{ls} \pm \sigma_d$, respectively) with the red lines showing the measured rate (E_m) and uncertainty derived from ^{10}Be samples collected in 2006, 2012, and 2015/2016 (from left to right panel); lower panel shows the background denudation rate (E_b ; blue lines) as a function of the fraction of landslide sediments (F_{ls}) according to the ^{10}Be sample derived rate (E_m). Orange shading shows the permissible range of background erosion rate for the case that E_b remains constant over 2001-2016. See text for more details on this approach.

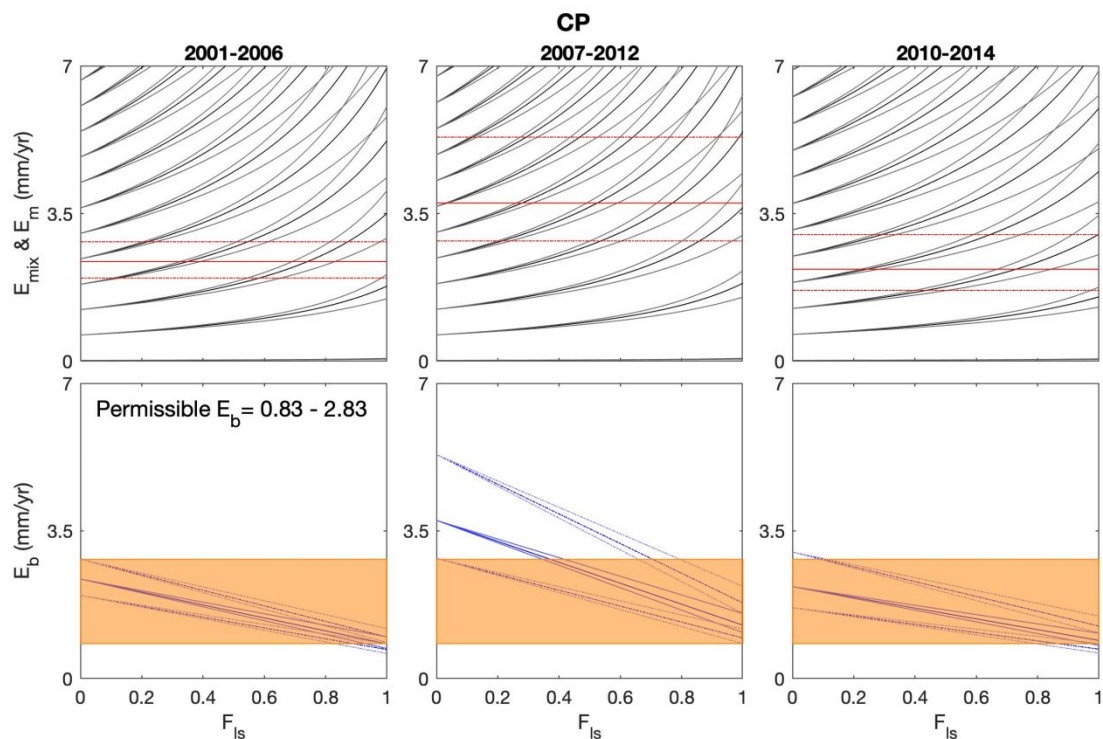


Fig. S2 Result of sediment-mixing model of the CP basin. Format as in Figure S1.

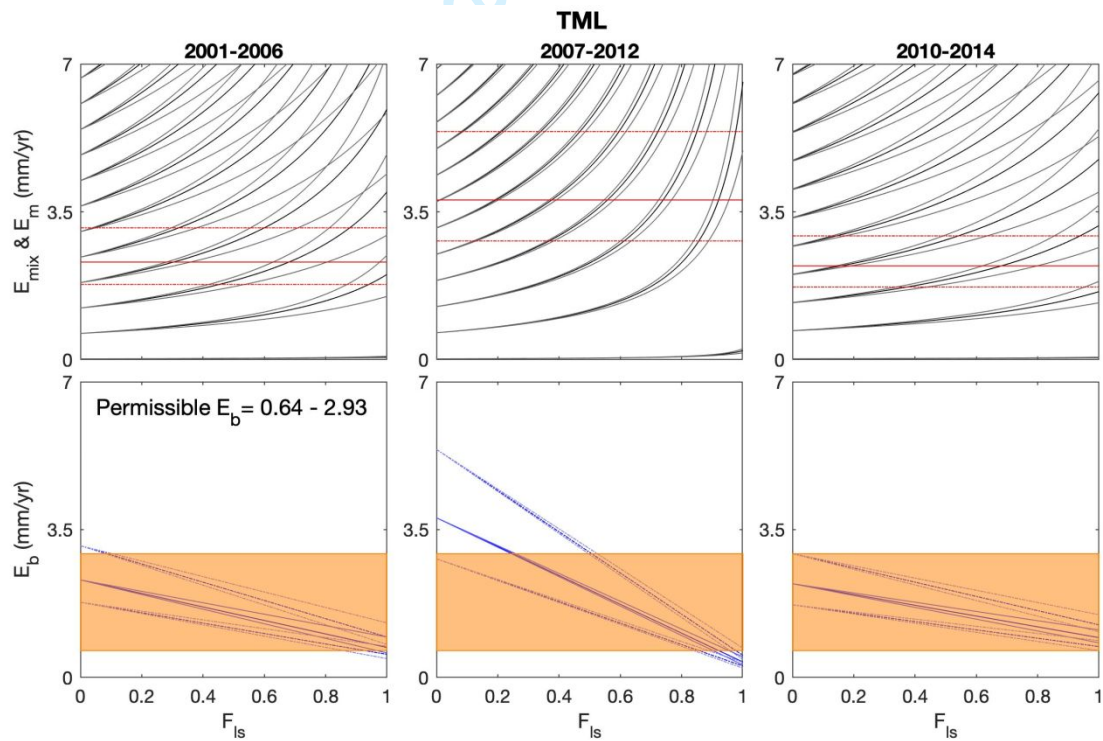


Fig. S3 Result of sediment-mixing model of the TML basin. Format as in Figure S1.

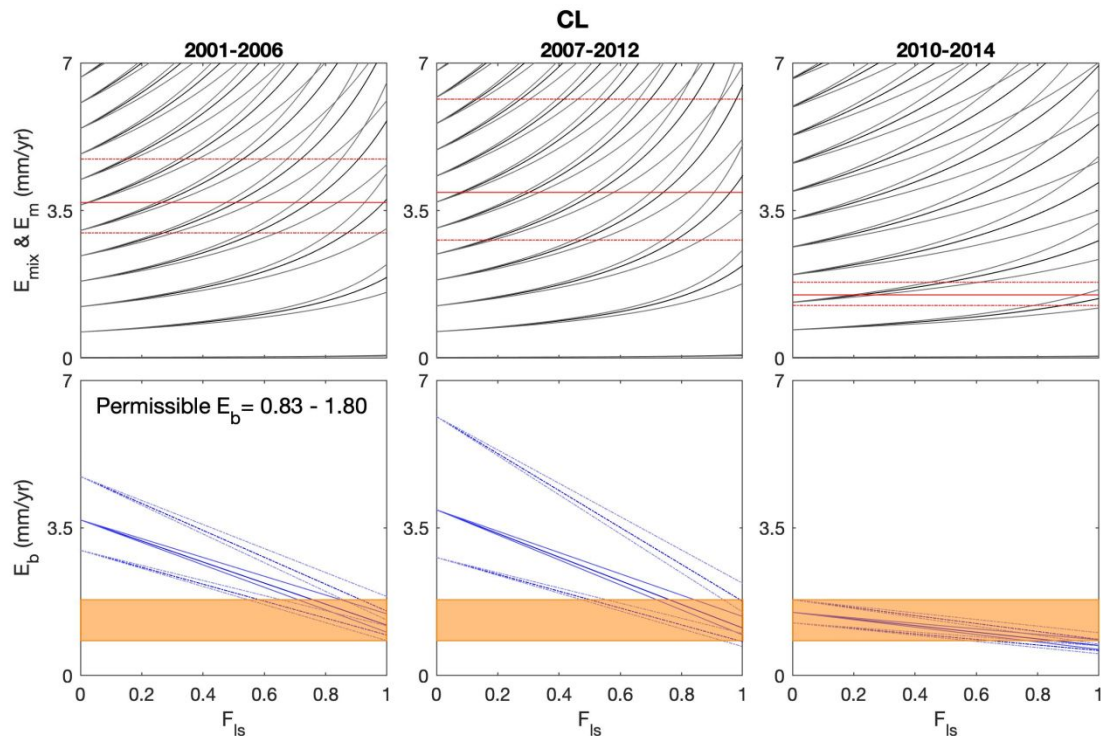


Fig. S4 Result of sediment-mixing model of the CL basin. Format as in Figure S1.

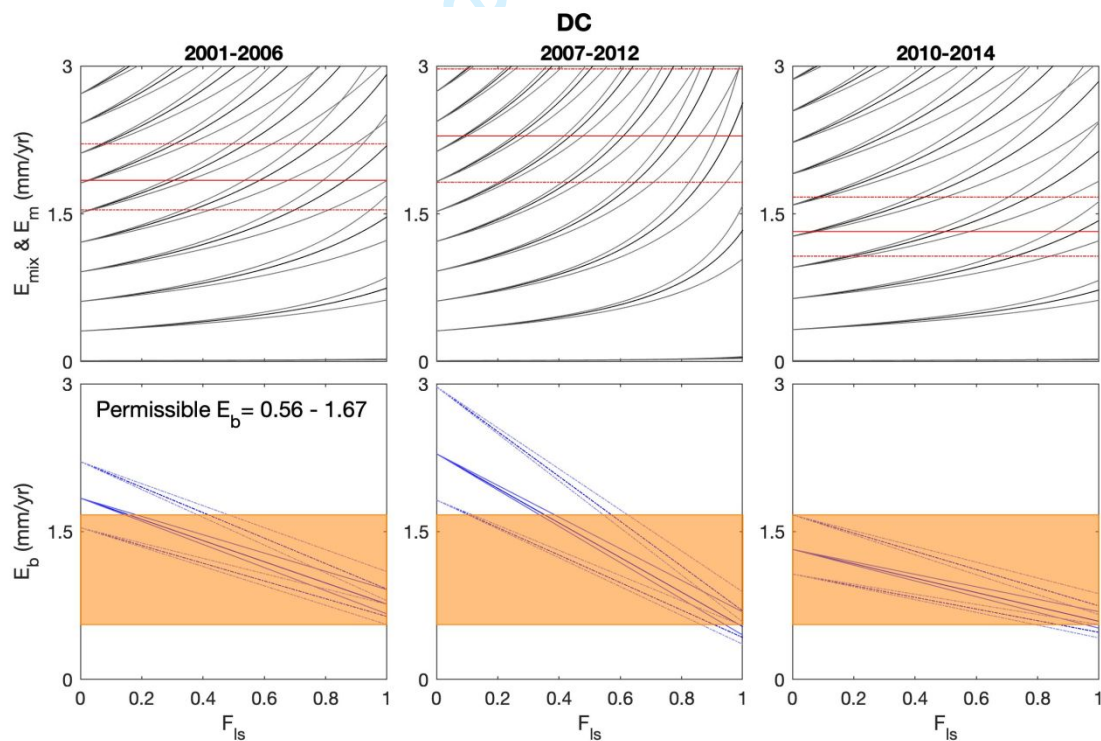


Fig. S5 Result of sediment-mixing model of the DC basin. Format as in Figure S1.

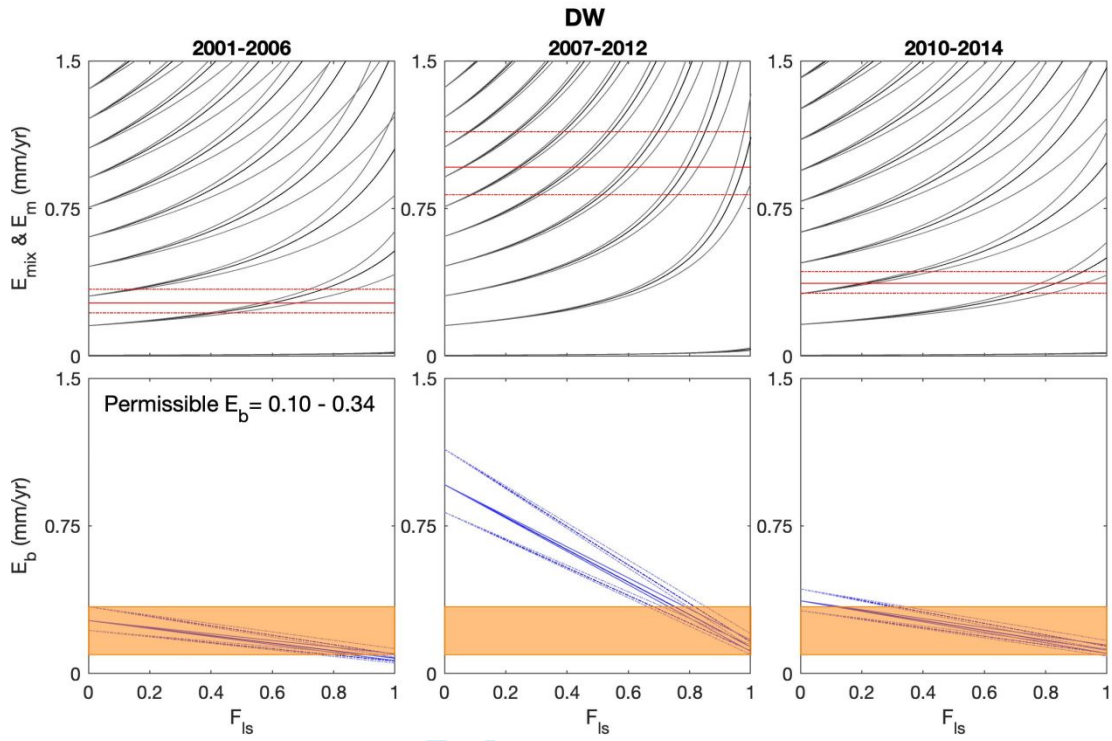


Fig. S6 Result of sediment-mixing model of the DW basin. Format as in Figure S1.

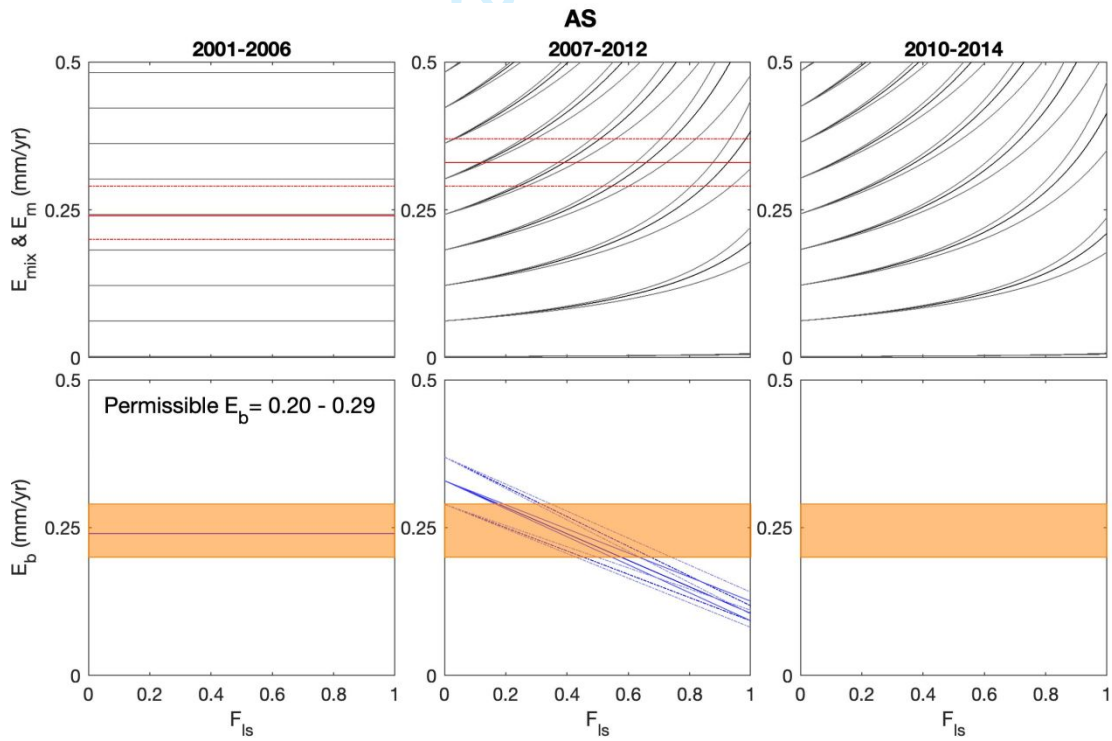


Fig. S7 Result of sediment-mixing model of the AS basin. Format as in Figure S1. There were no landslides mapped over the period of 2001-2006, and thus E_{mix} equals to E_m in any given F_{ls} . E_m measured in 2006 was assumed to be E_b and used to constrain the value of F_{ls} over the period of 2007-2012. There was no sample collected for estimated the erosion rate in 2015/2016, so there are no E_m and E_b determined over the period of 2010-2014.

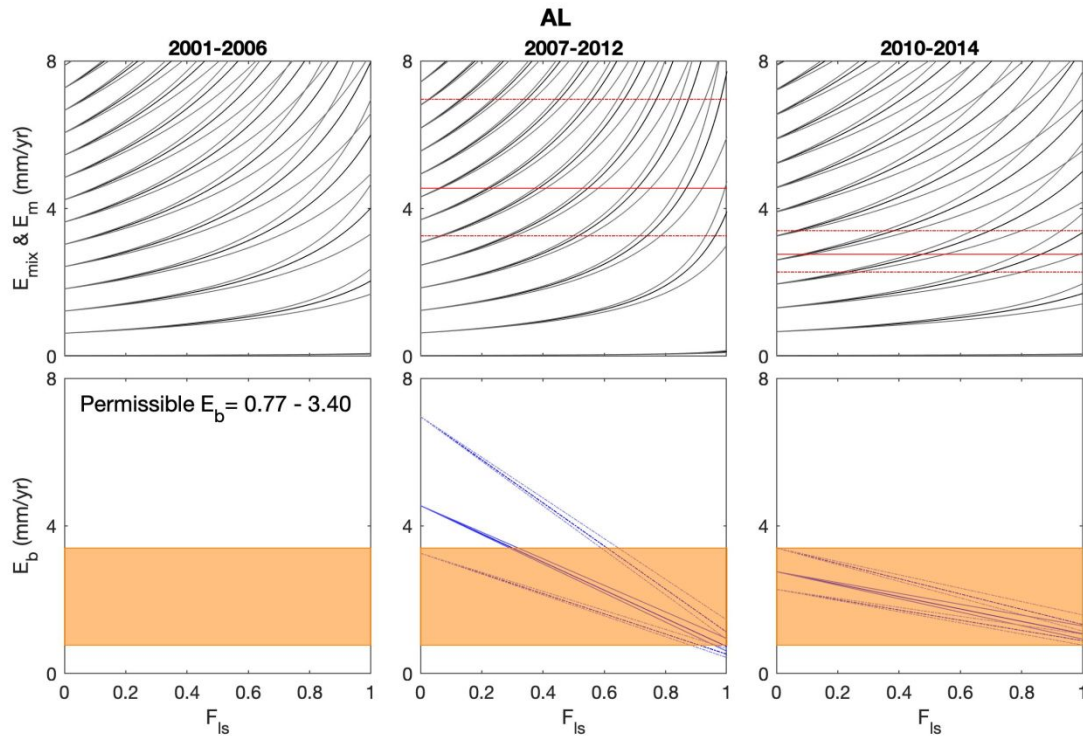


Fig. S8 Result of sediment-mixing model of the AL basin. Format as in Figure S1. There was no sample collected for estimated the erosion rate in 2006, so there are no E_m and E_b determined over the period of 2001-2006.

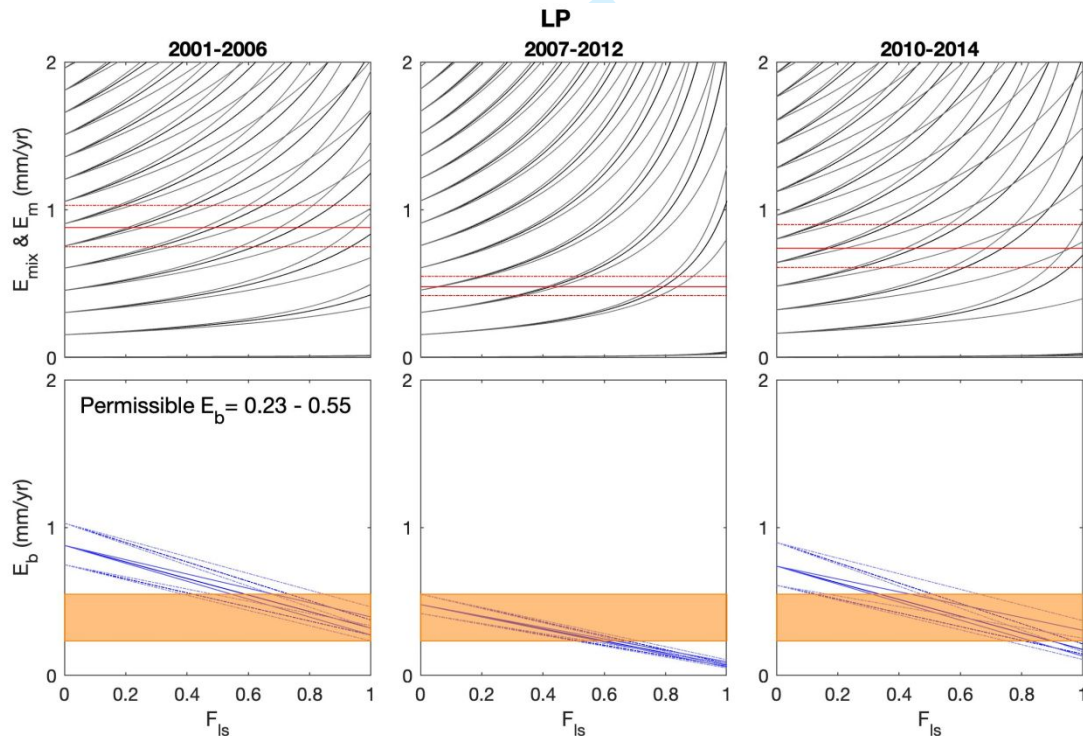


Fig. S9 Result of sediment-mixing model of the LP basin. Format as in Figure S1.

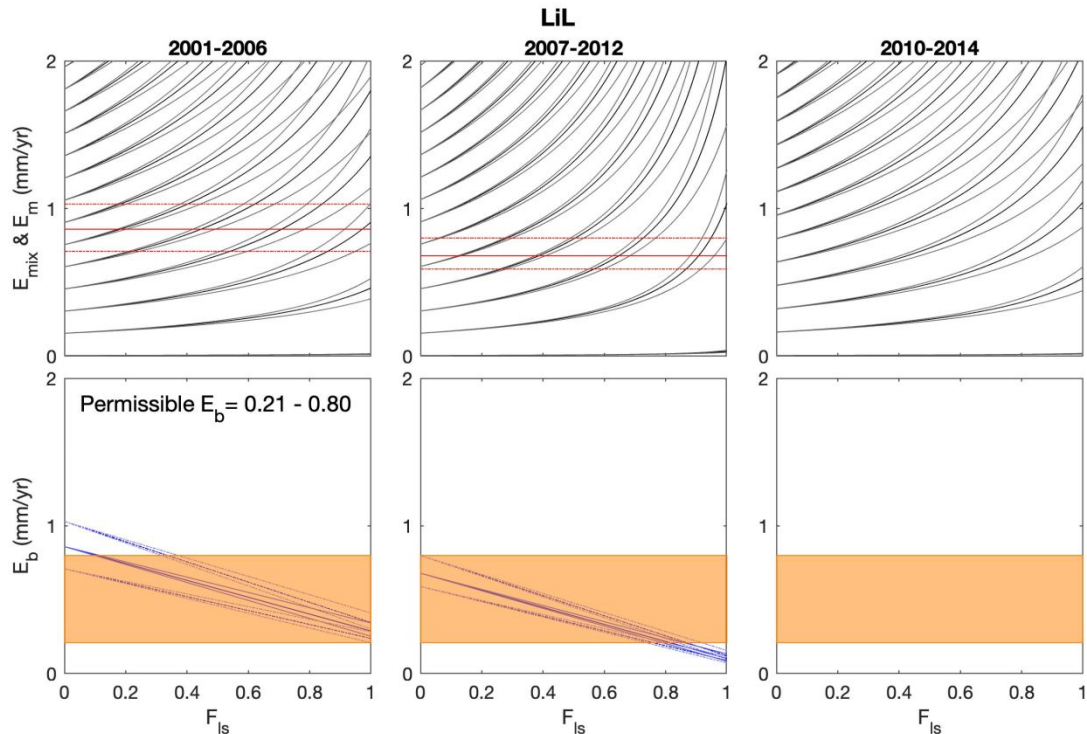


Fig. S10 Result of sediment-mixing model of the LiL basin. Format as in Figure S1. There was no sample collected for estimated the erosion rate in 2015/2016, so there are no E_m and E_b determined over the period of 2010-2014.

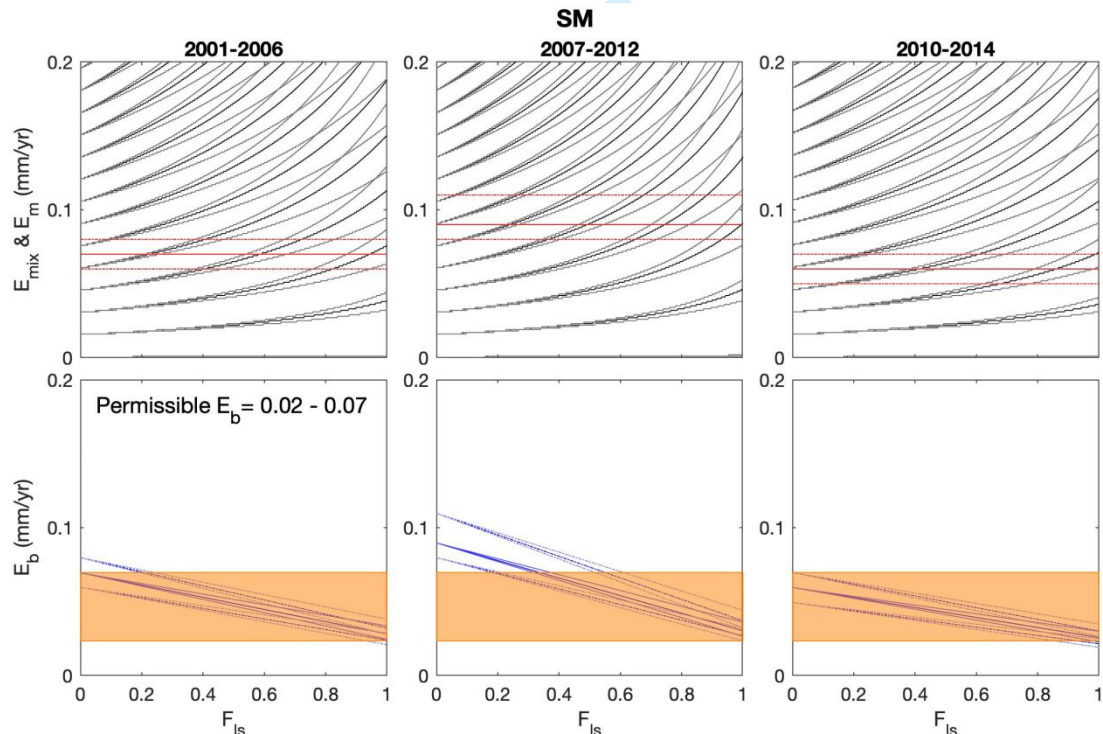


Fig. S11 Result of sediment-mixing model of the SM basin. Format as in Figure S1.

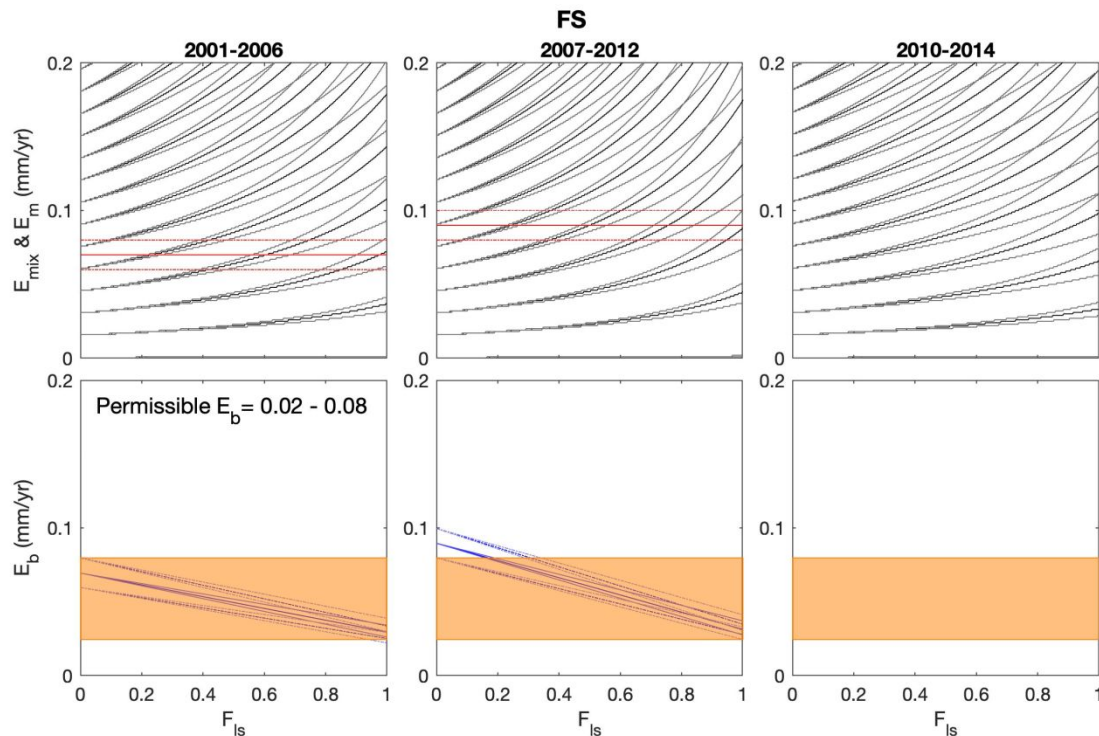


Fig. S12 Result of sediment-mixing model of the FS basin. Format as in Figure S1. There was no sample collected for estimated the erosion rate in 2015/2016, so there are no E_m and E_b determined over the period of 2010-2014.

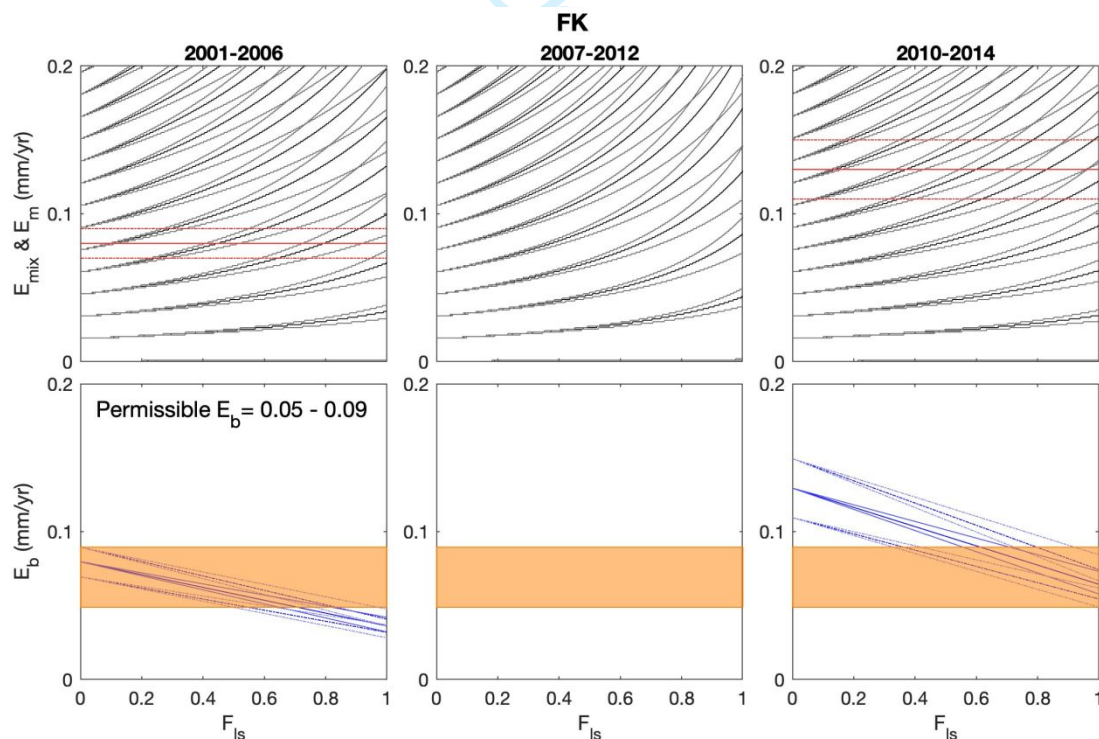


Fig. S13 Result of sediment-mixing model of the FK basin. Format as in Figure S1. There was no sample collected for estimated the erosion rate in 2012, so there are no E_m and E_b determined over the period of 2007-2012.

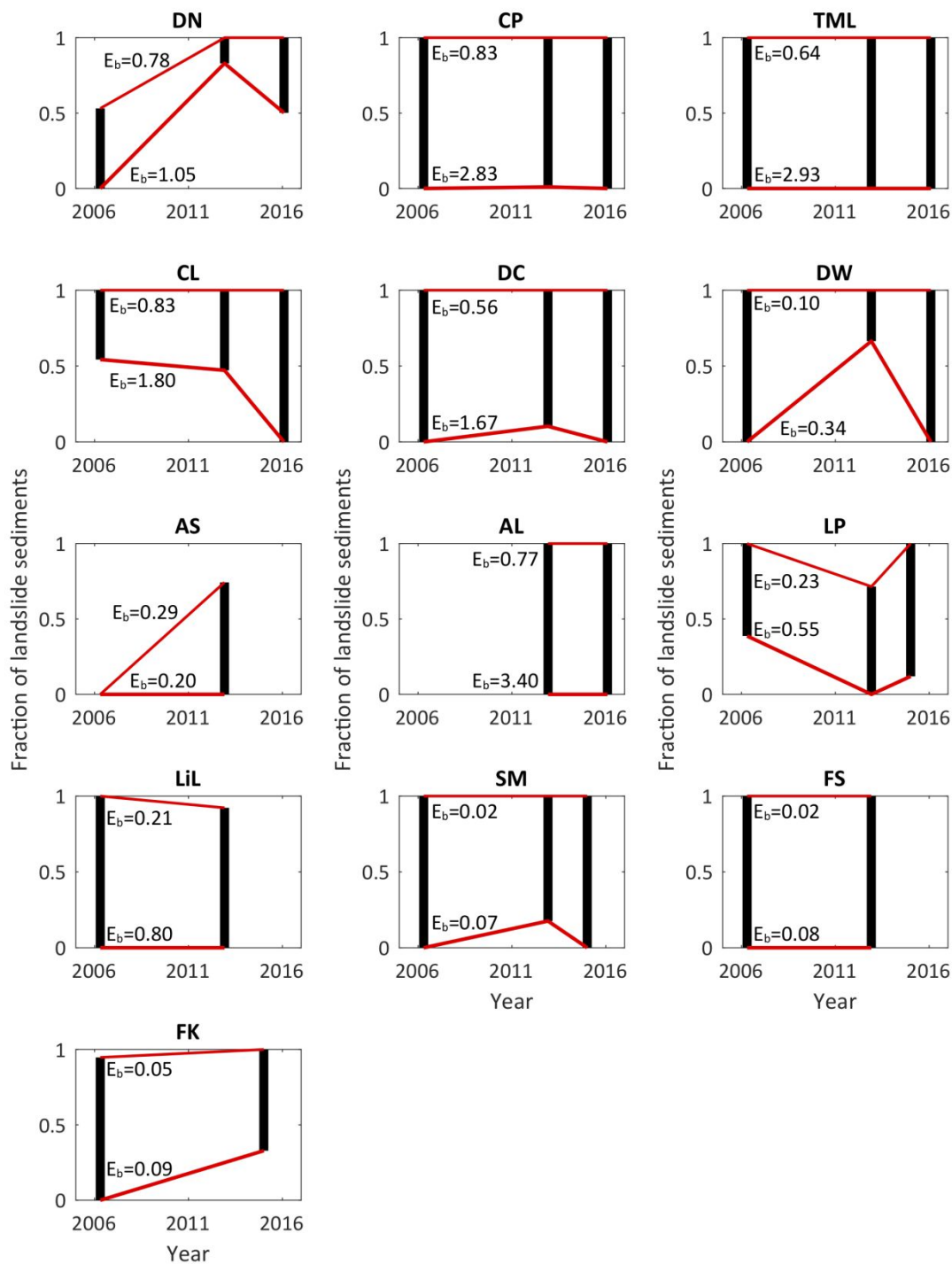


Fig. S14 Plots show temporal variations in fraction of landslide sediments (F_{ls}) estimated from the sediment-mixing model. In each plot, the black bar shows the permissible range of F_{ls} provided by landslides across the time interval of the study; the upper and lower solid red lines show the lower and upper limits of background denudation rate (E_b). Values of E_b are reported in mm/yr.

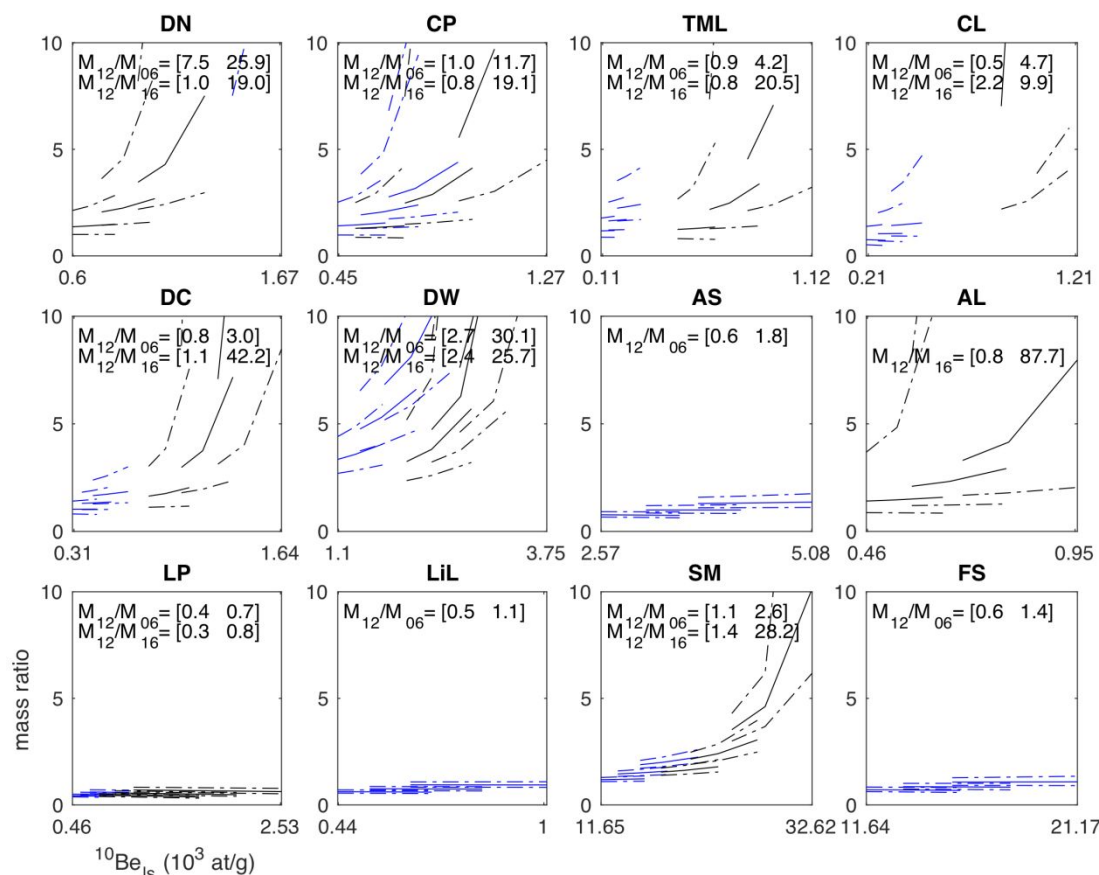


Fig. S15 Plots show the ratio of sediment mass in 2012 to the mass in 2006 (in blue) and 2016 (in black) as a function of the mean ^{10}Be concentration in landslide sediments ($^{10}\text{Be}_{\text{Is}}$). The ratio is calculated based on an end-member mixing: $M_2/M_1 = (^{10}\text{Be}_1 - ^{10}\text{Be}_{\text{Is}})/(^{10}\text{Be}_2 - ^{10}\text{Be}_{\text{Is}})$ following West et al., (2014). For M_{12}/M_{06} and M_{12}/M_{16} , we calculated $^{10}\text{Be}_1$ by assuming erosion rates equal to the rates derived from samples collected in 2006 and 2016, respectively. $^{10}\text{Be}_2$ is the concentration measured from the 2012 sample, and $^{10}\text{Be}_{\text{Is}}$ is the mean ^{10}Be concentration in landslide sediments calculated based on $^{10}\text{Be}_1$ and landslide depths (see text). Uncertainties in landslide depths and ^{10}Be -derived rates in two different years were considered, so for the ratio between two years, we obtained 9 solid and dashed lines in each basin; all lines are shown on the plots. Values in brackets show the ranges of the mass ratios. We did not collect a sample from the FK basin in 2012, so we cannot calculate the mass ratio for this basin.

Table S1

Correlation coefficient (R) and p-value of each linear regression in Figure 3, showing the strength of the relationship between ^{10}Be concentration (C) and areal density of landslides (LAD) in different cases. Subscripts s and d denote shallow and deep landslides, respectively.

Year	LAD		LAD _s		LAD _d		Note
	R	p-value	R	p-value	R	p-value	
2006	-0.48	0.13	-0.49	0.13	-0.10	0.94	
2012	-0.50	0.10	-0.50	0.10	0.52	0.19	
2015/2016	-0.48	0.16	-0.46	0.18	-	-	
2006	-0.47	0.24	-0.53	0.18	-0.10	0.94	excluding basins FS, SM, and FK
2012	-0.27	0.45	-0.41	0.24	0.52	0.19	
2015/2016	-0.60	0.12	-0.61	0.11	-	-	
2006	-0.49	0.33	-0.55	0.26	-0.10	0.94	excluding basins FS, SM, FK, LP, and LiL
2012	-0.55	0.16	-0.58	0.13	0.06	0.91	
2015/2016	-0.55	0.20	-0.55	0.20	-	-	

Table S2

Correlation coefficient (R) and p-value of each linear regression in Figure 4, showing the strength of the relationship between normalized changes in ^{10}Be concentration, and normalized changes in scar area ($N\Delta\text{IsA}$) and volume ($N\Delta\text{IsV}$) of landslides. Subscripts s and d denote shallow and deep landslides, respectively.

		$N\Delta\text{IsA}$	$N\Delta\text{IsA}_s$	$N\Delta\text{IsA}_d$	$N\Delta\text{IsV}$	$N\Delta\text{IsV}_s$	$N\Delta\text{IsV}_d$
2006 vs 2012	R	0.17	0.14	0.98	-0.13	0.15	-0.63
	p-value	0.68	0.74	0.12	0.76	0.73	0.56
2006 vs 2015/2016	R	-0.3	-0.34	-	-0.38	-0.46	-
	p-value	0.47	0.41	-	0.36	0.25	-

Table S3

Results of the sediment-mixing model test in the DN basin, showing the variations of the range of background erosion rate (E_b) with different changes in mean background $N^{10}\text{Be}$ (\bar{N}_b) and mean $N^{10}\text{Be}$ in landslide sediments (\bar{N}_{ls}).

Change of \bar{N}_b (%)	Change of \bar{N}_{ls} (%)	Range of E_b (mm/yr)
100 (no change)	100	0.78-1.05
100	80	0.63-1.05
90	80	0.70-1.05
80	80	0.78-1.05
80	90	0.88-1.05
80	100	0.98-1.05

100	110	0.86-1.05
100	120	0.94-1.05

Reference

West AJ, Hetzel R, Li G, Jin Z, Zhang F, Hilton RG, Densmore AL. 2014. Dilution of ^{10}Be in detrital quartz by earthquake-induced landslides: Implications for determining denudation rates and potential to provide insights into landslide sediment dynamics. *Earth and Planetary Science Letters* **396** : 143–153. DOI: 10.1016/j.epsl.2014.03.058

For Peer Review

The impact of storm-triggered landslides on sediment dynamics and catchment-wide denudation rates in the southern Central Range of Taiwan following the extreme rainfall event of Typhoon Morakot

Chia-Yu Chen*, Sean D. Willett, A. Joshua West, Simon Dadson, Niels Hovius, Marcus Christl and J. Bruce H. Shyu

The 2009 typhoon Morakot triggered thousands of landslides in southern Taiwan, causing a substantial increase in landslide areal density. Morakot-associated landslide material led to dilution of ¹⁰Be in river sediments, resulting in temporal variations in ¹⁰Be derived erosion rate. Background erosion rates were estimated with a sediment-mixing model, and the resultant spatial pattern of erosion rate reveals the early collision stage of the orogen.

